Title: OGDHL regulates tumor growth, neuroendocrine marker expression, and nucleotide abundance in prostate cancer

Authors: Matthew J. Bernard[1], Angel Ruiz[1], Johnny A. Diaz[1], Nicholas M. Nunley[2], Rachel N. Dove[2], Shile Zhang[3], Ernie Lee[2], Kylie Y. Heering[2], Sachi Bopardikar[2], Andrea Gallardo[2], Takao Hashimoto[2], Raag Agrawal[4,5], Chad M. Smith[2], Blake R. Wilde[5,6], Nedas Matulionis[6], Helen M. Richards[7], Sandy Che-Eun S. Lee[8], Marina N. Sharifi[9,10], Joshua M. Lang[9,10], Shuang G. Zhao[9,11,12], Michael C. Haffner[7,13,14], David B. Shackelford[5,8], Paul C. Boutros[4, 5, 15], Heather R. Christofk[5, 6, 16] , Andrew S. Goldstein[2,5,15,16,*]

Affiliations:

1. Molecular Biology Interdepartmental Program, University of California, Los Angeles, Los Angeles, CA 90095, USA
2. Department of Molecular, Cell, and Developmental Biology, University of California, Los Angeles, Los Angeles, CA 90095, USA
3. Department of Molecular and Medical Pharmacology, David Geffen School of Medicine, University of California, Los Angeles, Los Angeles, CA 90095, USA
4. Department of Human Genetics, University of California, Los Angeles, Los Angeles, CA 90095, USA
5. Jonsson Comprehensive Cancer Center, University of California, Los Angeles, Los Angeles, CA 90095, USA
6. Department of Biological Chemistry, David Geffen School of Medicine, University of California, Los Angeles, Los Angeles, CA 90095, USA
7. Division of Human Biology, Fred Hutchinson Cancer Center, Seattle, WA 98109, USA
8. Pulmonary and Critical Care Medicine, David Geffen School of Medicine, University of California Los Angeles, Los Angeles, CA 90095, USA.
9. Carbone Cancer Center, University of Wisconsin-Madison, Madison, WI 53792, USA
10. Department of Medicine, University of Wisconsin-Madison, Madison, WI 53792, USA
11. Department of Human Oncology, University of Wisconsin, Madison, WI 53792, USA

12. William S. Middleton Veterans Hospital, Madison, WI 53792, USA

13. Division of Clinical Research, Fred Hutchinson Cancer Center, Seattle, WA 98109, USA

14. Department of Laboratory Medicine and Pathology, University of Washington, Seattle, WA 98109, USA

15. Department of Urology, David Geffen School of Medicine, University of California, Los Angeles, Los Angeles, CA 90095, USA

16. Eli and Edythe Broad Stem Cell Research Center, University of California, Los Angeles, Los Angeles, CA 90095, USA

* To whom correspondence should be addressed: AGoldstein@mednet.ucla.edu

Abstract

As cancer cells evade therapeutic pressure and adopt alternate lineage identities not commonly observed in the tissue of origin, they likely adopt alternate metabolic programs to support their evolving demands. Targeting these alternative metabolic programs in distinct molecular subtypes of aggressive prostate cancer may lead to new therapeutic approaches to combat treatment-resistance. We identify the poorly studied metabolic enzyme Oxoglutarate Dehydrogenase-Like (OGDHL), named for its structural similarity to the tricarboxylic acid (TCA) cycle enzyme Oxoglutarate Dehydrogenase (OGDH), as an unexpected regulator of tumor growth, treatment-induced lineage plasticity, and DNA Damage in prostate cancer. While OGDHL has been described as a tumor-suppressor in various cancers, we find that its loss impairs prostate cancer cell proliferation and tumor formation. Loss of OGDHL profoundly alters Androgen Receptor inhibition-induced plasticity, including suppressing the neuroendocrine markers DLL3 and HES6, induces accumulation of the DNA damage response marker γH2AX, and reduces nucleotide synthesis. Our data suggest that OGDHL has minimal impact on TCA cycle activity, and that mitochondrial localization is not required for its regulation of prostate cancer plasticity and nucleotide metabolism. Finally, we demonstrate that OGDHL expression is tightly correlated with neuroendocrine differentiation in clinical prostate cancer. These findings underscore the importance of investigating poorly characterized metabolic genes as potential regulators of distinct molecular subtypes of aggressive cancer.

56 **Introduction**

57 Cells constantly undergo rapid metabolic changes to respond to external stimuli or local nutrient availability, and
58 to meet biosynthetic demands[1]. This ability to quickly overhaul metabolic networks allows healthy cells to
59 properly integrate signaling, regulate redox homeostasis, and modulate epigenetic substrates that dictate cell
60 fate decisions[2,3]. Due to differences in bioenergetic and metabolite pool needs, these networks are fine tuned in
61 a cell-type specific manner. During oncogenic transformation and disease progression, cancer cells hijack
62 cellular metabolism to evade therapeutic and biological pressures[4,5]. There is a growing appreciation for the
63 reciprocal relationship between cellular lineage and metabolism[6–8]. Perturbation of these metabolic switches
64 dramatically alters cell identity and differentiation. One major function of metabolic enzymes is to generate
65 energy and fuel anabolic growth. In addition, recent findings have indicated that many of these same enzymes
66 also serve non-canonical functions that more directly regulate transcriptional profiles and cellular signaling[9–12].

67

68 Prostate cancer is one of the most common cancers globally, accounting for nearly 1.5 million new cases
69 annually[13]. In the United States alone, there will be more than 35,750 deaths in 2025[14]. Identifying novel
70 strategies for the treatment of advanced prostate cancer is essential for improving outcomes for patients with
71 prostate cancer. Because Androgen Receptor (AR) signaling can promote survival and proliferation of tumor
72 cells[15], most advanced prostate cancers are treated with hormonal therapies that target the AR signaling axis,
73 including Enzalutamide and Apalutamide that directly bind and inhibit AR. While AR inhibitors have improved
74 patient survival for individuals with CRPC[16,17], disease recurrence is nearly universal. One mechanism through
75 which tumor cells adapt to AR blockade is through changes in lineage identity that result in AR-indifferent
76 tumors[18]. Despite recent promising clinical trial results[19], tumors that become resistant to AR blockade currently
77 lack many effective therapeutic options and are almost uniformly lethal[20]. Understanding how cells adapt to AR
78 inhibition and drive resistant phenotypes is essential for developing new therapies for patients with advanced
79 treatment-resistant prostate cancer.

80

81 We previously demonstrated that castration-resistant prostate cancer (CRPC) cells undergo extensive metabolic
82 remodeling in response to prolonged AR inhibition using the antiandrogen drug Enzalutamide[21]. Notably, cells
83 adapting to sustained AR blockade exhibit altered mitochondrial morphology and increased reliance on

84 mitochondrial oxidative metabolism. In prostate cancer, metabolic rewiring occurs concomitantly with the
85 activation of AR-independent lineage programs to evade pharmacological targeting, including acquisition of
86 neuronal, neuroendocrine (NE), and stem-like features[22–26]. We know little about whether treatment-induced
87 changes in metabolism directly regulate treatment-induced plasticity phenotypes, and which enzymes may be
88 involved in this process. The mitochondria serve as a central hub for both bioenergetic production and metabolite
89 pool regeneration, while also influencing cell signaling[27]. Disruption of metabolite pools can induce apoptosis,
90 alter cell fate, and exacerbate cancer progression through the accumulation of oncometabolites. One metabolic
91 enzyme associated with mitochondrial function is Oxoglutarate Dehydrogenase-Like (OGDHL), an isozyme of
92 Oxoglutarate Dehydrogenase (OGDH), which catalyzes the rate-limiting step in the interconversion of alpha-
93 ketoglutarate (a-KG) into succinyl-CoA within the tricarboxylic acid (TCA) cycle. While OGDH is expressed
94 robustly throughout nearly every cellular lineage in the body, OGDHL expression is primarily localized to the
95 brain and liver[28,29]. OGDHL is expressed in various cancer types and displays tumor suppressor properties in
96 kidney, cervical, and pancreatic cancers[30–35]. Despite its aberrant expression across these multiple cancers, our
97 understanding of the function of OGDHL remains poorly characterized. In a few studies, OGDHL has been
98 suggested to modulate immune signaling, lipid metabolism, and DNA damage[30,34,35].
99
100 Replication of DNA for proliferation is a strictly regulated process due to the deleterious nature of most mutations.
101 High fidelity replication of nearly 3 billion base pairs is required each time a cell proliferates. Because of this, the
102 DNA repair pathway is critical to maintain cell health and proper proliferation. Many of the most commonly altered
103 tumor suppressor genes, including *Tp53*, *Brca2*, and *Rb1*, are regulators of the DNA damage response and/or
104 serve as cell cycle checkpoints[36–38]. Mutations in these critical genes can usurp the DNA damage regulatory
105 mechanisms and unleash unchecked cell growth, resulting in a more frequent mutation rate and increased
106 susceptibility to oncogenic transformation[39]. Cells accumulate the metabolite precursors required for DNA
107 synthesis through several mechanisms including salvage of ribonucleotides and deoxyribonucleotides from the
108 surrounding microenvironment and through *de novo* synthesis pathways[40]. Rewiring of these metabolic
109 pathways through alternative means during biological and therapeutic pressures serves as one way tumor cells
110 adapt to sustain tumor growth[41]. Precise regulation of these nucleotide pools is paramount for proper RNA and
111 DNA synthesis and repair pathways. Imbalance of these pools can induce replication stress, leading to cell cycle

112 arrest and apoptosis. Dysregulation of nucleotide pools has also been linked to altered lineage differentiation,
113 which is associated with sensitivity or resistance to targeted therapies. In summary, the intersection of metabolic
114 rewiring and nucleotide metabolism represents an intriguing target for the treatment of aggressive and therapy-
115 resistant cancer subtypes.
116
117 Here, we identify the TCA cycle enzyme OGDHL as a regulator of tumor cell proliferation and treatment-induced
118 lineage plasticity in prostate cancer. OGDHL is elevated in a group of prostate cancer cell lines, patient-derived
119 xenograft (PDX) models, genetically engineered mouse models, and clinical tissues from patients with
120 aggressive, lethal treatment-resistant prostate cancer. Unlike in prior reports of other cancer-types, we did not
121 find evidence for OGDHL as a tumor suppressor or as a regulator of the TCA cycle. Instead, loss of OGDHL
122 expression impairs cell proliferation and tumor formation. We demonstrate that chronic loss of OGDHL restrains
123 the treatment-associated plasticity in response to prolonged AR pathway inhibition, reducing expression of NE
124 markers HES6 and DLL3. Loss of OGDHL induces accumulation of the DNA damage marker γH2AX and
125 reduces nucleotide synthesis, resulting in depleted nucleotide pools. Mechanistically, we found that OGDHL
126 function does not require mitochondrial localization to maintain its role in regulation of lineage marker expression
127 and nucleotide metabolism in prostate cancer.
128
129

Results

OGDHL regulates cell proliferation and tumor growth in castration-resistant prostate cancer

Having established that prolonged AR inhibition induces a metabolic shift characterized by increased reliance on mitochondrial oxidative metabolism *in vitro*[21], we evaluated the effect of AR blockade on tumor cell metabolism *in vivo* using a multi-tracer Positron Emission Tomography (PET) imaging strategy. We generated xenograft tumors from MDA-PCa 180-30[42] cells in NOD-SCID-IL2Rg^{null} (NSG) mice and treated with enzalutamide via daily oral gavage for 2 weeks. To define treatment-induced changes in tumor metabolism *in vivo*, we first conducted radiolabeled tracing using ^{18}F-FBnTP-PET to measure mitochondrial membrane potential as an indicator of oxidative capacity. Twenty-four hours later, we performed ^{18}F-FDG-PET to measure glucose uptake as a surrogate for glycolytic activity. Enzalutamide treatment induced a statistically significant reduction in ^{18}F-FDG signal (**Figure 1A)**, while ^{18}F-FBnTP signal was not significantly different (**Figure 1B**), indicating that enzalutamide treatment also induces a metabolic shift toward mitochondrial oxidative metabolism *in vivo*. Two weeks of Enzalutamide treatment in MDA-PCa 180-30 tumor-bearing mice was sufficient to reduce tumor size and weight (**Figure S1, S1B)**. As we determined that increased reliance on mitochondrial oxidative metabolism was a consequence of AR blockade *in vitro* and *in vivo*, we evaluated transcriptional changes in TCA cycle enzymes following extended (> 6 weeks) Enzalutamide treatment. OGDHL was the most enriched enzyme, exhibiting a greater than 2-fold increase in mRNA expression in Enzalutamide-maintained cells compared to control 16D^{CRPC} cells (**Figure 1C**). We next verified that OGDHL protein expression was elevated in response to Enzalutamide treatment and found that this upregulation of OGDHL did not correspond to a compensatory downregulation of the homologous OGDH (**Figure 1D**). OGDHL protein expression was roughly 30% greater in Enzalutamide-treated MDA-PCa 180-30 CRPC tumors relative to vehicle-treated control tumors (**Figure 1E, 1F)**.

Although the precise physiological role of OGDHL in the TCA cycle has not been well defined, OGDHL has been investigated as a prognostic biomarker for multiple cancers[43,44] and is reported to have tumor-suppressive activity in cervical, pancreatic, kidney, and liver cells[30–35]. To investigate the role of OGDHL in prostate cancer, we maintained three parallel sub-lines of 16D^{CRPC} cells in Enzalutamide to allow them to independently adapt to prolonged AR inhibition. OGDHL protein levels increased in each of these lines and this expression increased

158 over time as cells adapted to AR blockade (**Figure S1C**). OGDHL expression was also increased in response to
159 AR inhibition in two independent *in vitro* models of CRPC: LuCAP35^{CR} cells grown in 2D culture, and MDA-PCa
160 180-30[42] organoids (**Figure S1D, S1E)**. To determine the functional role of OGDHL in prostate cancer, we
161 generated constitutive overexpression systems in several prostate cancer cell line models (**Figure S1F**). Forced
162 expression of OGDHL had no impact on tumor cell viability in LNCaP, 16D^{CRPC} or PC3 cells (**Figure 1G**).
163 Because increased OGDHL expression seemed to be a consistent cellular response to prolonged AR blockade,
164 we next evaluated how loss of OGDHL influences proliferation. Short hairpin RNA (shRNA)-mediated knockdown
165 of OGDHL in Enzalutamide-maintained 16D^{CRPC} and LuCAP35^{CR} cells significantly reduced cell viability (**Figure**
166 **1H, S1G-I**). We implanted control and knockdown cells in Matrigel to generate 3D tumoroids and found that
167 OGDHL knockdown significantly reduced tumoroid size, an indicator of proliferative capacity (**Figure 1I, 1J**).
168
169 To evaluate the effect of OGDHL loss on tumor formation, we implanted control and OGDHL knockdown
170 Enzalutamide-maintained 16D^{CRPC} cells with Matrigel into NSG mice and quantified outgrowths after 4 weeks *in*
171 *vivo*. Tissues recovered from implantation of OGDHL knockdown cells were significantly smaller. Recovered
172 tissues had an average mass of 26.26 +/- 36.24 mg (shOGDHL #1) and 11.34 +/- 5.57 mg (shOGDHL #2)
173 compared to 41.86 +/- 23.67 mg in scrambled control tissues (**Figure 1K, 1L).** Most of the tissues derived from
174 knockdown cells lacked visible outgrowths, so we quantified the percentage of recovered tissues weighing more
175 than the Matrigel alone. Only 33.3% (5/15) of tissues resected from OGDHL knockdown xenografts weighed
176 more than the injection medium alone, compared to 100% (15/15) of tissues resected from control cells (p =
177 0.0002), suggesting that OGDHL knockdown cells fail to efficiently grow *in vivo*. We validated reduced protein
178 abundance of OGDHL in the recovered tissues from knockdown cells (**Figure S1J**). Interestingly, one outgrowth
179 from OGDHL knockdown cells was greater than five times heavier than any other OGDHL knockdown tissue,
180 suggesting that in rare instances, cells can overcome OGDHL loss to form tumors *in vivo*. Taken together, our
181 data suggest that OGDHL does not act as a tumor-suppressor in CRPC, as has been shown in other cancer
182 contexts. These findings indicate that OGDHL supports CRPC growth *in vitro* and tumor-forming capacity *in vivo*.
183
184 **OGDHL loss suppresses cell cycle-related signatures *in vitro* and *in vivo***

185 Because the role of OGDHL in CRPC seems to differ from its reported function in other cancers, we investigated
186 the effect of OGDHL loss on gene expression by conducting RNA-sequencing in Enzalutamide-Maintained
187 $16D^{CRPC}$ cells. We first asked whether OGDHL loss induces compensatory changes in the expression of closely
188 related TCA cycle enzymes. We found minimal changes in expression of canonical TCA cycle genes (**Figure**
189 **2A**) or a broader list of TCA cycle-associated genes (**Figure S2A**) in response to acute OGDHL loss. We next
190 took an unbiased approach to determine broad transcriptional changes induced by acute knockdown of OGDHL.
191 Significantly upregulated genes were associated with cell stress pathways, including *GADD45A*, *CASP4*, and
192 *TP53INP2*. Significantly downregulated genes were associated with cell cycle and proliferation, such as *CDC20*,
193 *CENPN*, *MYC*, and *TOP2A* (**Figure 2B, 2C**). Gene Set Enrichment Analysis (GSEA) revealed strong
194 downregulation of cell cycle signatures, including the Hallmark gene sets for G2M checkpoint, E2F targets, and
195 Myc Targets at both the gene set and individual gene level (**Figures 2E, S2B**). To confirm results obtained using
196 shRNA-mediated knockdown, we used a CRISPR-Cas9 approach to generate independent OGDHL knockout
197 $16D^{CRPC}$ cell lines that are maintained in Enzalutamide. After validating the knockout cells by Western blot (**Figure**
198 **S2C**), we found that chronic loss of OGDHL did not induce compensatory upregulation of TCA cycle genes
199 (**Figures S2D, S2E**). Similar to acute knockdown of OGDHL, genetic knockout of OGDHL led to a pronounced
200 reduction in G2M checkpoint genes, E2F target genes, and Myc target genes (**Figure 2E**). We implanted OGDHL
201 knockout and control cells in castrated NSG mice to maintain suppression of AR signaling *in vivo* and performed
202 RNA sequencing upon tumor formation. After validating loss of OGDHL protein (**Figure S2F**), we found a strong
203 transcriptional downregulation of G2M checkpoint, E2F targets, and Myc Target genes in knockout cells *in vivo*
204 (**Figure 2F**). Taken together, these data indicate that loss of OGDHL in AR inhibition-resistant CRPC cells
205 represses transcription of cell cycle associated genes and activates transcriptional pathways related to cellular
206 stress.
207

208 **OGDHL regulates nucleotide biosynthesis in Enzalutamide-treated castration-resistant prostate cancer**

209 Due to the unexpected effect of OGDHL loss on transcription of proliferation and cellular stress genes, we next
210 set out to determine the metabolic function of OGDHL in prostate cancer cells. OGDHL is predicted to form a
211 complex with dihydrolipoyl succinlyltransferase (DLST) and dihydrolipoyl dehydrogenase (DLD) to catalyze the
212 conversion of alpha-ketoglutarate (a-KG) into succinyl-CoA in the TCA cycle[45]. To measure changes in nutrient

213 utilization, we conducted heavy-isotope nutrient tracing experiments using U-^{13}C Glucose and U-^{13}C Glutamine
214 for 24 hours (**Figure 3A**) in Enzalutamide-Maintained 16D^{CRPC} cells following OGDHL knockdown. OGDHL loss
215 did not lead to an accumulation of heavy-isotope labeled a-KG (**Figure 3B**) or a reduction in labeled carbons
216 downstream of a-KG from either glucose or glutamine (**Figure S3A-S3C**). These findings suggest that OGDHL
217 plays a limited role in regulating the incorporation of glucose or glutamine-derived metabolites into the TCA cycle
218 in CRPC cells, possibly due to the functional redundancy with OGDH.
219
220 We next attempted to identify other metabolic consequences of acute OGDHL loss. Many of the significantly
221 depleted metabolites were involved in pyrimidine biosynthesis and nucleotide homeostasis (**Figure 3C**). Across
222 multiple biological replicates of Enzalutamide-maintained prostate cancer cells, OGDHL loss consistently led to
223 a depletion of nucleotide phosphates (**Figure 3D**) and reduced abundance of certain biosynthetic intermediates
224 of nucleotide synthesis including Phosphoribosyl pyrophosphate (PRPP) and dihydroorotate **(Figure 3E, 3F**).
225 Glucose can be incorporated into *de novo* synthesized nucleotides through conversion to a ribose backbone via
226 the pentose phosphate pathway (**Figure 3A**). We found that acute OGDHL loss reduced carbon labeling from
227 glucose into newly synthesized nucleotides phosphates, including both pyrimidines **(Figure 3G)** and purines
228 **(Figure S3D).** This reduction in labeling was concurrent with a reduction in nucleotide pools, consistent with
229 decreased activity of the pentose phosphate pathway and diminished *de novo* nucleotide synthesis.
230
231 To understand how chronic loss of OGDHL influences cellular metabolism, we conducted heavy-isotope nutrient
232 tracing experiments in OGDHL knockout cell lines. When we tracked glucose incorporation into the TCA cycle,
233 we found that labeling of a-KG was similar to labeling of other TCA cycle intermediates (**Figure S3E).** Further,
234 OGDHL knockout did not alter labeling from glutamine into the TCA cycle, through either the oxidative (**Figure**
235 **S3F**) or reductive carboxylation (**Figure S3G)** pathways. Much like in response to acute knockdown, metabolic
236 profiling of OGDHL knockout cells revealed a reduction in abundance of ribonucleotides and
237 deoxyribonucleotides (**Figure S3H**). Taken together, our metabolomic data indicate that the main metabolic
238 consequence of OGDHL loss in CRPC cells is not altered TCA cycle metabolism, but rather depletion of
239 nucleotide pools, at least in part through slowed *de novo* nucleotide synthesis.
240

241 **OGDHL regulates DNA repair and cell stress pathways in prostate cancer**

242 Nucleotide imbalance has a profound impact on cellular proliferation, cell cycle progression, and DNA damage
243 machinery[46]. As we found that loss of OGDHL diminished nucleotide pools and reduced glucose incorporation
244 into newly synthesized nucleotides, we evaluated expression of nucleotide metabolism genes. Genetic knockout
245 of OGDHL *in vitro* and *in vivo* reduced expression of critical *de novo* nucleotide synthesis and salvage genes
246 including Carboamoyl-Phosphate Synthase 2 (*CAD*), Dihydroorotate Dehydrogenase (*DHODH*), Uridine
247 monophosphate synthetase (*UMPS*), Hypoxanthine phosphoribosyltransferase 1 (*HPRT1)* and Adenine
248 phosphoribosyl transferase (APRT) (**Figure 4A, 4B, S4A, S4B**). More broadly, OGDHL knockout reduced
249 expression of genes in the KEGG Pyrimidine Metabolism gene set (**Figure 4C**). Similarly, we found that acute
250 knockdown of OGDHL in Enzalutamide-maintained $16D^{CRPC}$ cells reduced transcription of *de novo* pyrimidine
251 synthesis and purine salvage genes (**Figure S4C)**. These data indicate that diminished nucleotide abundance
252 following the loss of OGDHL expression in CRPC is likely caused by impaired *de novo* synthesis and nucleotide
253 salvage.

254

255 Depletion of nucleotides can cause genomic instability and trigger replication stress, leading to double stranded
256 DNA breaks, cell cycle arrest and apoptosis[47,48]. OGDHL has been implicated as a potential regulator of DNA
257 damage in cancer[35,49]. Thus, we wondered whether loss of OGDHL may cause increased replication stress.
258 Acute knockdown of OGDHL led to increased transcription of genes in the Hallmark Apoptosis gene set and
259 reduced expression of DNA repair pathway genes (**Figure 4D, 4E).** In addition to transcriptional hallmarks of
260 replication stress, we also identified that knockdown of OGDHL *in vitro* led to increased abundance of γH2AX
261 (**Figure 4F**), a sensitive marker of double stranded DNA breaks and a hallmark of DNA damage[50]. We similarly
262 observed an increase in γH2AX when OGDHL knockdown cells were grown *in vivo* (**Figure 4G, 4H, S4E**). We
263 confirmed that OGDHL knockdown induces DNA damage using a comet assay based on single cell gel
264 electrophoresis (**Figure S4F**). OGDHL loss also reduced expression of the DNA repair pathway genes CHK1
265 and CHK2 (**Figure S4G).** As DNA damage can induce cell death, we questioned whether OGDHL loss induced
266 higher rates of apoptosis. We found that OGDHL loss increased the percentage of Annexin V^+ cells (**Figure S4H)**.
267 To confirm that these phenotypes are driven by OGDHL loss, we introduced a knockdown-resistant version of
268 OGDHL and found that the rescue reduced markers of DNA damage including DNA tail length by the comet

assay and γH2AX (**Figure S4F, S4I**). We wondered whether OGDHL-loss induced DNA damage accumulation and apoptosis could be related to depletion of nucleotides. Supplementation with Adenine (A) and Uridine (U) led to reduced apoptosis in the most sensitive knockdown group **(Figure S4H).** These data suggest that loss of OGDHL in CRPC reduces nucleotide availability, through reduction of nucleotide synthesis and salvage genes, and increases replication stress.

OGDHL regulates expression of neuroendocrine markers *in vitro* and *in vivo*

Prolonged AR blockade can induce changes in cell identity as tumor cells adopt AR-indifferent cell fates to adapt to treatment pressure[51]. This process, known as lineage plasticity, can give rise to aggressive and uniformly lethal molecular subtypes, such as neuroendocrine prostate cancer (NEPC)[18]. Because changes in cell fate rely on proper nucleotide balance and DNA damage repair[52,53], we questioned whether loss of OGDHL may alter treatment-induced lineage phenotypes in prostate cancer cells. To understand how OGDHL influences response to prolonged AR blockade, we generated OGDHL knockout lines in $16D^{CRPC}$ cells, then treated them with Enzalutamide for 6 weeks. RNA-sequencing revealed that prolonged Enzalutamide treatment of control cells led to increased expression of genes associated with plasticity phenotypes including Axon Guidance, WNT Signaling, Epithelial-mesenchymal transition, and decreased expression of Androgen Response genes. In contrast, OGDHL knockout impaired the AR blockade-induced upregulation of plasticity-associated gene sets (**Figure 5A-5C, S5A**). Canonical indicators of lineage plasticity and antiandrogen-resistance, including upregulation of *ENO2* (encoding NSE) and *SOX9*[54], were abrogated by loss of OGDHL (**Figure S5B, S5C**). OGDHL knockout *in vitro* led to a strong reduction in expression of *HES6* (**Figure 5D)**, an evolutionarily conserved driver of neuronal development[55–57], NE differentiation and lineage plasticity in prostate cancer[58–62]. OGDHL knockout also reduced expression of HES6 target genes[63] (**Figure S5D**). We questioned whether this reduction in NE markers was a consequence of persistent OGDHL loss or could be induced by acute knockdown of OGDHL. We found that knockdown of OGDHL in Enzalutamide-maintained $16D^{CRPC}$ cells *in vitro* reduced protein expression of HES6 (**Figure S5E)** and transcription of HES6 targets (**Figure S5F),** suggesting that reduced NE marker expression is a consistent feature of OGDHL loss.

296 We next sought to understand if OGDHL loss could influence lineage plasticity phenotypes *in vivo.* Knockout
297 tumors grown in castrated mice showed statistically significant reductions in transcription of NEPC genes *HES6*
298 and *DLL3* (**Figure 5E, 5F)**. OGDHL knockout tumors also showed significantly reduced expression of HES6
299 target genes and other gene sets associated with AR blockade-induced plasticity phenotypes (**Figure 5G, S5G,**
300 **S5H**). HES6 protein expression was also reduced following OGDHL knockdown *in vivo* (**Figure 5H, S5I, S5J)**
301 indicating that OGDHL loss modulates expression of NEPC markers *in vitro* and *in vivo*. In summary, these data
302 suggest that OGDHL influences AR-blockade induced lineage plasticity phenotypes.
303

304 **Mitochondrial localization is not required for OGDHL-mediated regulation of nucleotide synthesis and**
305 **lineage phenotypes**

306 Metabolic enzymes involved in various processes, including the TCA cycle, have been shown to localize to the
307 nucleus to modulate chromatin and regulate gene expression[9–12,64–66]. As we found that OGDHL loss impacted
308 AR blockade-induced lineage phenotypes, we attempted to revert these transitions through restoration of
309 OGDHL. In OGDHL knockout cells, we reintroduced OGDHL with a silent mutation in the CRISPR targeted
310 sequence. To assess the effect of mitochondrial and non-mitochondrial function, we generated both a full-length
311 version (FL) and one lacking the mitochondrial targeting sequence (ΔMTS) (**Figure 6A**). We validated protein
312 expression (**Figure 6A**) and the localization of each variant (**Figure 6B**). While the FL variant displayed strong
313 colocalization with the mitochondrial marker TUFM, the ΔMTS variant displayed a diffuse, non-mitochondrial
314 signal (**Figure 6B, S6A**). We next evaluated nuclear and mitochondrial OGDHL signal in these rescue
315 backgrounds and the localization of endogenous OGDHL in our Enzalutamide-maintained $16D^{CRPC}$ cells (**Figure**
316 **6C**) via immunofluorescence. Endogenous OGDHL localization exhibited an average 40 +/- 17.5% overlap with
317 mitochondrial signal and an average 51+/- 24.7% overlap with nuclear (DAPI) signal (**Figure 6D, 6E**).
318 Importantly, we validated a significant reduction in mitochondrial signal, and significant increase in nuclear signal
319 overlapping with the ΔMTS mutant compared to FL (**Figure 6D, 6E**).
320

321 Bulk RNA-sequencing demonstrated that restoration of OGDHL increased transcriptional expression of genes
322 in pyrimidine metabolism, HES6 target genes, and cell cycle associated gene sets (**Figure 6F-H, S6B, & S6C**).
323 This increase was more pronounced in cells lacking the mitochondrial targeting sequence, indicating the non-

324 mitochondrial function of OGDHL may be more important for its impact on gene expression. At the protein level,
325 restoration of FL and/or ΔMTS OGDHL was sufficient to abrogate OGDHL knockdown induced phenotypes
326 including reductions in MYC and the nucleotide synthesis enzyme TK1, as well as γH2AX accumulation (**Figure**
327 **S6D**). To assess the impact on cell metabolism, we conducted heavy-isotope glucose tracing. Consistent with
328 our earlier findings that OGDHL does not play a meaningful role in regulating the TCA cycle, OGDHL
329 reintroduction had limited influence on glucose incorporation into TCA cycle metabolites (**Figure S6E**).
330 Restoration of OGDHL with either FL or ΔMTS variants increased glucose incorporation into newly synthesized
331 pyrimidines including Uridine Phosphates (**Figure 6I**) and Cytidine Phosphates (**S6F**). Taken together, these
332 data indicate that mitochondrial localization is not required for OGDHL-mediated regulation of lineage identity
333 and nucleotide synthesis in prostate cancer.
334
335 **OGDHL expression is associated with neuroendocrine differentiation in prostate cancer**
336
337 As we found that OGDHL loss influenced treatment-associated lineage phenotypes, we next set out to identify
338 the expression pattern of OGDHL in advanced prostate cancer. We first interrogated TCA cycle enzyme
339 expression in a series of murine models of prostate cancer progression driven by loss of tumor suppressors
340 *Pten*, *Rb1* and *Tp53*[67]. Notably, the combined loss of *Pten* and *Rb1* (double knockout, DKO) or all three genes
341 together (triple knockout, TKO) promotes a loss of luminal features and a gain of markers associated with NEPC.
342 Among all TCA cycle genes evaluated, OGDHL was the most prominently associated with disease progression
343 and plasticity (**Figure 7A**). OGDHL expression was greater than 10-fold higher in the NEPC-like TKO (Rb1
344 null;Tp53-null;PTen-null) tumors compared to the more luminal-like Pten-knockout tumors (**Figure 7B**). We next
345 questioned whether this correlation with prostate cancer plasticity was also observed in clinical human prostate
346 cancer and in patient-derived xenograft tumors. In RNA sequencing data collected from clinical CRPC patients[68],
347 we found that OGDHL expression was nearly 15-fold higher in patients with NEPC compared to CRPC-
348 adenocarcinoma (**Figure 7C).** In the Stand Up 2 Cancer metastatic CRPC dataset[69,70], OGDHL expression was
349 highest in tumors with NE features, regardless of AR expression/activity, while OGDHL expression was lowest
350 in tumors lacking NE features (**Figure 7D)**. Similar results were observed in the University of Washington rapid
351 autopsy metastatic cohort[71] (**Figure 7E)** and in the LuCAP PDX series[72] (**Figure 7F)** where OGDHL expression
352 was highest in the NE+ AR- subset of tumors. Sharifi *et al.* recently defined mCRPC phenotypes based on RNA

353 sequencing of circulating tumor cells, demonstrating that NE and LumB subtypes are associated with the shortest
354 overall survival[73]. We found that OGDHL mRNA was detectable in CTCs and its expression was highest in the
355 NE+ and LumB subtypes (**Figure 7G**). To ensure OGDHL was not suppressed by AR, we evaluated OGDHL
356 expression in prostate cancer patients treated with Androgen Deprivation Therapy (ADT)[74–76]. We found that
357 OGDHL expression was reduced in patients following ADT treatment in both paired and unpaired data sets
358 (**Figure S7A-S7C).** Collectively, these data suggest that OGDHL is not specifically associated with AR
359 repression but rather with plasticity and NE differentiation in CRPC.
360

361 **Discussion**

362 In this study, we demonstrate that the putative TCA cycle enzyme OGDHL is elevated at the mRNA and protein
363 levels in response to prolonged AR blockade in CRPC cells. Despite its reported function as a tumor-suppressor
364 gene in other cancers[30–35], we find that OGDHL promotes antiandrogen resistant prostate cancer cell proliferation
365 *in vitro* and *in vivo*. While some genes play a consistent role either in suppressing or driving tumorigenesis, many
366 cancer-associated genes have context-dependent functions where they provide protective benefits in some
367 cancer subtypes, while promoting disease progression in others. Among these are epigenetic remodelers such
368 as EZH2 and KDM5A[77–79], signaling factors such as TGFβ[80], and metabolic genes such as PDHA1 and AMPK[81–
369 83]. Our findings suggest that OGDHL represents a context-dependent regulator of cancer progression, promoting
370 cell survival and adaptation to therapeutic pressures in prostate cancer.
371

372 Although the TCA cycle generates intermediate metabolites and biosynthetic precursors to enable metabolic and
373 cellular functions and sustain cell growth, there is a growing appreciation for non-canonical roles of TCA cycle
374 enzymes. Many metabolic enzymes, including the OGDH complex, have been reported to display nuclear
375 localization to rapidly replenish metabolite pools for epigenetic reprogramming, despite their predominant
376 expression in other subcellular compartments[9–12,64–66,84]. Metabolites, including those generated through TCA
377 cycle enzymes, are critical substrates for epigenetic regulatory proteins, enabling the deposition and removal of
378 methyl, acetyl, and succinyl marks on histone tails[2,8,85]. This enables cells to rapidly adapt to changes in nutrient
379 availability, respond to extracellular signaling, and promote cell fate decisions. Because of this interconnectivity,
380 there is a reciprocal relationship between cellular metabolism and lineage identity. OGDH complex activity

modulates levels of two metabolites that are essential for faithful regulation of differentiation programs. a-KG is a critical intermediate for epigenetic regulation, as it is an obligate substrate for a class of demethylase enzymes called a-KG dependent dioxygenases (KGDDs)[86]. Alternatively, the product of OGDH complex activity, succinyl-CoA, can be used to succinylate lysine residues on histone tails, resulting in changes in chromatin accessibility and gene expression[87,88]. Here, we demonstrate that OGDHL modulates mRNA and protein expression of NEPC markers including DLL3 and HES6, suggesting that OGDHL may promote disease progression in CRPC at least in part through gene regulation. In support of that idea, modulation of OGDHL expression does not markedly alter glucose or glutamine incorporation into TCA cycle intermediates. Instead, OGDHL loss potently depletes nucleotide pools and glucose incorporation into nucleotides, while reducing expression of enzymes that fuel nucleotide synthesis and salvage.

Proper maintenance of nucleotide pools is essential to enable proliferation, gene expression, and DNA damage repair[89]. Accumulation of nucleotides is especially important for the proliferation of tumor cells due to their rapid proliferative demands, thus representing a specific vulnerability. Because of this, nucleotide metabolism is a major target for many clinically deployed cancer therapeutics[90]. However, rewiring of nucleotide metabolism in cancer can facilitate pharmacological resistance and immune cell evasion[91–93]. We find that OGDHL loss in antiandrogen-resistant prostate cancer cells depletes nucleotide pools and induces accumulation of γH2AX, a prominent marker of replication stress. These findings are consistent with a previous report that utilized bioinformatic approaches to implicate OGDHL as a potential DNA damage-resistance gene in prostate cancer[48]. Interestingly, OGDHL overexpression has been reported to modulate nucleotide pools and induce DNA damage in hepatocellular carcinoma, thereby inhibiting disease progression[35]. This highlights the unique function of OGDHL in prostate cancer progression. In addition to accumulation of γH2AX, we find that OGDHL loss reduces transcription of cell cycle associated genes and increases transcription of apoptotic and cellular stress response genes. We postulate that OGDHL is elevated in response to prolonged AR blockade in order to promote nucleotide homeostasis, which enables sustained proliferation and treatment-induced lineage plasticity. As OGDHL is not highly expressed in benign prostate tissue or localized disease, but is consistently elevated in NEPC, OGDHL may represent a novel therapeutic target for this currently uniformly lethal prostate cancer subtype.

While our findings highlight the importance of OGDHL in cell survival and lineage plasticity in prostate cancer, many questions remain. Although OGDHL modulates nucleotide metabolism, tumor growth, DNA damage response, and plasticity in CRPC, the mechanisms underlying these roles are still unclear. It is possible OGDHL plays a direct role in epigenetic regulation through enzymatic function in the nucleus, regulating a-KG and succinyl-CoA levels to modulate DNA methylation, histone methylation, and histone succinylation. As the OGDH complex does not directly modulate intermediates of *de novo* nucleotide synthesis, more direct mechanistic studies to uncover how OGDHL regulates nucleotide metabolism will be essential. OGDHL is a poorly characterized homolog of a much more broadly expressed and investigated metabolic gene, therefore more careful exploration of the nuances differentiating these two, as well as identifying targetable motifs on OGDHL, are important to clarify its potential as a therapeutic target for currently untreatable prostate cancer subtypes.

Materials and Methods

Materials Availability

This work did not generate new unique reagents.

Animal Work

All animal work was performed using IACUC approved protocols under the supervision of veterinarians from the Division of Laboratory Animal Medicine at UCLA.

This method refers to figures 1K, 1L, S1J, 4G, 4H, S4E, 5H, S5I, and S5J.

750K Enzalutamide-maintained $16D^{CRPC}$ cells with short-hairpin (shRNA) mediated knockdown of OGDHL or a control vector were implanted subcutaneously with 20 µL of growth factor-reduced Matrigel (Corning: CB-40230C) to form tumors. After 4 days, material was collected from 4 control and 4 knockdown injections and used to generate protein lysate (Short Term *in vivo*). The remaining injections were allowed to grow for 4 weeks, after which material was collected, weighed, and used to generate protein lysate.

This method refers to figures 2F, S2F, 4A, S4A, 5E-5G, S5G, and S5H.

Serial dilutions of 1M, 100K, 10K, and 1K $16D^{CRPC}$ cells with CRISPR-Cas9 mediated genetic knockout of OGDHL were implanted subcutaneously with 20 µL of growth factor-reduced Matrigel (Corning: CB-40230C). Once palpable tumors were measured in at least one mouse per condition (1M Cells: 6 Weeks; 100K Cells: 10 Weeks; 10K Cells: 12 Weeks, 1K cells: 16 Weeks), mice were sacrificed, tumors were resected, sectioned, and prepared as lysate or flash frozen for bulk RNA-sequencing.

This method refers to figure 1A, 1B, 1E, 1F, S1A, and S1B

550K MDa 180-30 PDX cells were implanted subcutaneously with 30 uL of growth factor-reduced Matrigel (Corning: CB-40230C). Tumors were allowed to establish for 19 days, then mice were treated with Enzalutamide or DMSO control via oral gavage daily for 14 days. *In vivo* tumor metabolism was then measured as describec below. After measurement of mitochondrial membrane potential and glucose consumption, mice were sacrificed, tumors were resected, sectioned, and prepared as lysate.

In Vivo Assessment of Tumor Cell Metabolism by ^{18}F-FBnTP and ^{18}F-FDG PET/CT

450 Animals without fasting were warmed on a heating pad for 30 min, anesthetized with 2% isoflurane in oxygen,
451 and injected via the tail vein with ~90 μCi of clinical-grade ^{18}F-fluorobenzyl-triphenylphosphonium (^{18}F-FBnTP)
452 or ^{18}F-fluorodeoxyglucose (^{18}F-FDG) in saline. Animals underwent a 1-hour conscious ^{18}F-FBnTP or ^{18}F-FDG
453 biodistribution period on a heating pad prior to imaging. Exact radiotracer isotope dose, draw time, time of
454 injection, and imaging start time were annotated to aid in signal normalization. Positron emission tomography
455 (PET) and computed tomography (CT) scans were conducted on a G8 combined PET/CT instrument (Sofie
456 Biosciences, Inc.) with a 600-s PET acquisition and maximum-likelihood expectation maximization
457 reconstruction, and with a 50-s CT acquisition and Feldkamp reconstruction. PET data were converted to
458 percent-injected dose per gram (%ID/g) and PET/CT images were co-registered. Mean values of PET signal
459 intensity from tumor region-of-interest (ROI) normalized to heart signal uptake were analyzed using AMIDE
460 software v1.0.4.
461
462 **Cell Lines, lentiviral transduction and cloning**
463 Cell Lines were routinely tested for mycoplasma and authentication by short tandem repeat analysis (Laragen).
464 Tissue culture plates were coated with 0.01% (v/v) Poly-L-Lysine Solution (Sigma-Aldrich: P4832) diluted 1:20
465 in ddH_2O, then washed with sterile DPBS without Calcium and Magnesium (Gibco: 14-190-20). $16D^{CRPC}$ and
466 LNCaP cells were cultured in RPMI 1640 (Gibco: 22400) supplemented with 10% (v/v) FBS (Sigma-Aldrich:
467 F0926), and 100 units/mL penicillin-streptomycin (Gibco: 15-140-122). Media changes were conducted every 48
468 hours and cells were passaged to fresh tissue culture plates once they reached 90% confluency. PC3 cells were
469 cultured in F-12K media (ATCC 30-2004) supplemented with 10% (v/v) FBS (Sigma-Aldrich: F0926), and 100
470 units/mL penicillin-streptomycin (Gibco: 15-140-122). LuCaP 35CR cells were cultured in Advanced DMEM F-
471 12 supplemented with 1% Glutamax (Gibco 35050061), 10% (v/v) FBS (Sigma-Aldrich: F0926), and 100
472 units/mL penicillin-streptomycin (Gibco: 15-140-122). Enzalutamide treatment was performed by adding 10μM
473 Enzalutamide (Selleck Chemicals: S1250) at each media change.
474
475 Lentivirus with short-hairpin RNA (shRNA) against OGDHL (shOGDHL) or a non-targeting control
476 (shScrambled), Cas9 Guide RNA (gRNAs) targeting OGDHL or an AAVS control, and OGDHL overexpression
477 vector were all obtained from Vectorbuilder (Chicago, IL, USA).

478

479 For Lentiviral transductions, cells were seeded at 30% confluence. After 24 Hours, base media containing
480 lentivirus and 8mg/mL Polybrene (ThermoFisher Scientific: NC0663391). Successful transduction was validated
481 by fluorescence microscopy (fluorescent vectors) or puromycin dihydrochloride selection (1.25 µg/mL) (Gibco:
482 A1113803), 72 H after infection.

483

484 **Tumoroid Culture**

485 This method refers to figure 1I and 1J

486 To generate tumoroids, cells were resuspended in a mixture of growth factor-reduced Matrigel (Corning: CB-
487 40230C) and culture media at a ratio of 7:1 to a density of 500 cells per 80 µL. This mixture was then added to
488 poly-hema coated 24-well culture plates (Corning: 09-761-146) as previously described[94]. Matrigel was allowed
489 to solidify at 37°C for 60 minutes, then 350 µL of RPMI 1640 (Gibco: 22400) supplemented with 10% (v/v) FBS
490 (Sigma-Aldrich: F0926), and 100 units/mL penicillin-streptomycin (Gibco: 15-140-122) was added to the center
491 of the solidified ring. Media was changed every other day. After 2 weeks, at least 50 tumoroids per condition
492 were imaged at 20X magnification and diameter was measured.

493

494 This method refers to Figure S1E

495 MDA-PCa 180-30[42] PDX tumors were maintained by serial implantation of 20 – 80 mg of minced tumor tissue.
496 Tumors were collected and cryopreserved. Upon thawing, tumor sections were mechanically dissociated and
497 embedded in Matrigel rings to establish *ex vivo* tumoroids. Tumoroids were maintained in Human Organoid
498 Media[95]. To passage tumoroids, media was removed and matrigel containing tumoroids was dissociated by
499 resuspension in Advanced DMEM-F12 (Gibco: 12-634-010) containing 1 mg/mL Dispase II (Gibco: 17-105-041)
500 and 10µM p160 ROCK-inhibitor Y-27632 2HCl (Selleck Chemicals: S1049). This mixture was incubated at 37°C
501 for 1 hour with constant rocking. Following dissociation, cells were pelleted by centrifugation at 800xG for 5
502 minutes, then resuspended in prewarmed 0.05% Trypsin-EDTA, Phenol Red (Gibco: 25-300-120) and pipetted
503 to homogenize. After 1 minute, media was added to quench the trypsinization, and cells were plated into Matrigel
504 rings as above. To treat with enzalutamide, Human organoid media containing 10 µM Enzalutamide was added
505 for 1 week, with fresh media supplied every other day.

506

507 ***In vitro* metabolic profiling and U-^{13}C isotope tracing**

508 This method refers to figures 3C-3F.

509 Enzalutamide-Maintained 16D cells harboring genetic knockdown (shRNA) OGDHL or a control vector were
510 seeded in a 6-well plate (Corning: 07-200-83) at 325K cells/well. After 48 hours, cells were washed with PBS,
511 then provided with glucose-free RPMI 1640 (Gibco: 11-879-020) supplemented with 11 mM U-^{13}C glucose
512 (Cambridge Isotope Labs: CLM-1396), 10% (v/v) FBS (Sigma-Aldrich: F0926), and 100 units/mL penicillin-
513 streptomycin (Gibco: 15-140-122).

514 24 hours after the addition of heavy-isotope labeled media was added, cells were harvested and extracted using
515 previously described methods[21]. In short, cells were placed on ice and washed with ice-cold 150 mM ammonium
516 acetate, pH 7.3, then immediately treated with 500 µL of 80% MeOH (v/v) containing 10nM
517 trifluoromethanesulfonate (internal standard). Cells were then scraped and transferred to a 1.7 mL
518 microcentrifuge tube, vortexed 3 times on ice then centrifuged at 17,000xg for 5 minutes. The supernatant was
519 transferred to ABC glass vials (DWK Life Sciences Wheaton 03-410-151) and dried using the EZ-2Elite
520 Evaporator (Genevac). Samples were stored at -80°C until analysis by LC-MS.

521

522 Dried metabolites were reconstituted in 100 µL of a 50% acetonitrile (ACN) 50% dH20 solution. Samples were
523 vortexed and spun down for 10 min at 17,000g. 70 µL of the supernatant was then transferred to HPLC glass
524 vials. 10 µL of these metabolite solutions were injected per analysis. Samples were run on a Vanquish (Thermo
525 Scientific) UHPLC system with mobile phase A (20mM ammonium carbonate, pH 9.7) and mobile phase B (100%
526 ACN) at a flow rate of 150 µL/min on a SeQuant ZIC-pHILIC Polymeric column (2.1 × 150 mm 5 µm, EMD
527 Millipore) at 35°C. Separation was achieved with a linear gradient from 20% A to 80% A in 20 min followed by a
528 linear gradient from 80% A to 20% A from 20 min to 20.5 min. 20% A was then held from 20.5 min to 28 min.
529 The UHPLC was coupled to a Q-Exactive (Thermo Scientific) mass analyzer running in polarity switching mode
530 with spray-voltage=3.2kV, sheath-gas=40, aux-gas=15, sweep-gas=1, aux-gas-temp=350°C, and capillary-
531 temp=275°C. For both polarities mass scan settings were kept at full-scan-range = (70-1000), ms1-
532 resolution=70,000, max- injection-time=250ms, and AGC-target=1E6. MS2 data was also collected from the top
533 three most abundant singly-charged ions in each scan with normalized-collision-energy=35. Each of the resulting

534 ".RAW" files was then centroided and converted into two ".mzXML" files (one for positive scans and one for
535 negative scans) using msconvert from ProteoWizard[96]. These ".mzXML" files were imported into the MZmine 2
536 software package[97]. Ion chromatograms were generated from MS1 spectra via the built-in Automated Data
537 Analysis Pipeline[98] (ADAP) chromatogram module and peaks were detected via the ADAP wavelets algorithm.
538 Peaks were aligned across all samples via the Random sample consensus aligner module, gap-filled, and
539 assigned identities using an exact mass MS1(+/-15ppm) and retention time RT (+/-0.5min) search of our in-
540 house MS1-RT database. Peak boundaries and identifications were then further refined by manual curation.
541 Peaks were quantified by area under the curve integration and exported as CSV files. If stable isotope tracing
542 was used in the experiment, the peak areas were additionally processed via the R package AccuCor 2[99] to
543 correct for natural isotope abundance. Peak areas for each sample were normalized by the measured area of
544 the internal standard trifluoromethanesulfonate (present in the extraction buffer) and by the number of cells
545 present in the extracted well.
546
547 This method refers to Figure 3B, 3G, S3A-S3H, 6I, S6E and S6F
548 Enzalutamide-Maintained 16D cells harboring genetic knockdown (shRNA), knockout (gRNA) of OGDHL, or a
549 combination of knockdown vector with a shRNA resistant- OGDHL expression vector, or a matched control vector
550 were seeded in a 6-well plate (Corning: 07-200-83) at 325K cells/well. After 48 hours, cells were washed with
551 PBS, then provided with glucose-free RPMI 1640 (Gibco: 11-879-020) supplemented with 11 mM U-^{13}C glucose
552 (Cambridge Isotope Labs: CLM-1396), 10% (v/v) FBS (Sigma-Aldrich: F0926), and 100 units/mL penicillin-
553 streptomycin (Gibco: 15-140-122) (for heavy-labeled glucose tracing) or glutamine-free RPMI 1640 (Gibco: 21-
554 870-076) supplemented with 2mM U-^{13}C glutamine (Cambridge Isotope Labs: CLM-1822) (for heavy-labeled
555 glutamine tracing), 10% (v/v) FBS (Sigma-Aldrich: F0926), and 100 units/mL penicillin-streptomycin (Gibco: 15-
556 140-122).
557 24 hours after the addition of heavy-isotope labeled media was added, cells were harvested and extracted using
558 previously described methods[21]. In short, cells were placed on ice and washed with ice-cold 150 mM ammonium
559 acetate, pH 7.3, then immediately treated with 500 µL of 80% MeOH (v/v) containing 1 nmol norvaline (internal
560 standard). Cells were then scraped and transferred to a 1.7 mL microcentrifuge tube, vortexed 3 times on ice
561 then centrifuged at 17,000xg for 5 minutes. The supernatant was transferred to ABC glass vials (DWK Life

562 Sciences Wheaton 03-410-151) and dried using the EZ-2Elite Evaporator (Genevac). Samples were stored at -
563 80°C until analysis by LC-MS.
564 To calculate cell number DNA normalization was performed by resuspending the insoluble fraction in 300 uL of
565 lysis solution (0.1M NaCl, 20mM Tris-HCL, 0.1% SDS, and 5mM EDTA in ddH_2O). Samples were then syringed
566 5x using a 25G needle to homogenize. 50uL of each sample was transferred into a 96-well black-walled clear
567 bottom plate (Corning: 07-200-588) and 100 uL of 5µg/mL Hoechst 33342 (ThermoFisher: H1399) in ddH_2O was
568 added. The plate was then incubated for 30 minutes at 37°C in the dark, after which DNA-based fluorescence
569 was measured using a Tecan Infinite M1000 plate reader with 355nm excitation and 465 emission.
570 Dried metabolites were resuspended in 50% ACN:water and 5 ul was loaded onto a Luna 3um NH2 100A (150
571 × 2.0 mm) column (Phenomenex). The chromatographic separation was performed on a Vanquish Flex (Thermo
572 Scientific) with mobile phases A (5 mM NH4AcO, pH 9.9) and B (ACN) and a flow rate of 200 µl/min. A linear
573 gradient from 15% A to 95% A over 18 min was followed by 7 min isocratic flow at 95% A and reequilibration to
574 15% A. Metabolites were detected with a Thermo Scientific Q Exactive mass spectrometer run with polarity
575 switching in full scan mode with an m/z range of 70-975 and 70.000 resolution. Maven (v 8.1.27.11) was utilized
576 to quantify the targeted metabolites by AreaTop using accurate mass measurements (< 5 ppm) and expected
577 retention time previously verified with standards.
578 Values were normalized to cell number. C13 natural abundance corrections were made using AccuCor[99] (N15
579 corrections are made with AccuCor, dual-labeled corrections are made with AccuCor2). Relative amounts of
580 metabolites were calculated by summing up the intensities of all detected isotopologues of a given metabolite.
581 Data analysis was performed using in-house R scripts.
582
583 **Cell Viability Assay**
584 This method refers to figures 1G, 1H, and S1I
585 Cell lines were detached from tissue culture plates using 0.05% Trypsin-EDTA, Phenol Red (Gibco: 25-300-120)
586 at 37°C for 5 minutes then quenched with culture medium, then pelleted by centrifugation, followed by
587 resuspension in base media. 10 µL of the resuspension was then mixed with Trypan Blue (Corning: 25900CI),
588 and cells were counted via hemocytometer.

589 Cells were seeded into duplicate 96-well black-walled clear bottom plate (Corning: 07-200-588) at a
590 concentration of 10K cells/well in 100 µL of base media. Each experiment was completed with between 4 and 6
591 technical replicates per condition. After 16 hours, 100 µL of CellTiter-Glo® Luminescent Cell Viability Assay
592 Reagent (Promega: G7571) was added, the plate was then incubated for 15 minutes at RT, on an orbital shaker.
593 Luminescence was measured using a Tecan Infinite M1000 plate reader with to obtain baseline values. 48 hours
594 later, 100 µL of CellTiter-Glo® Luminescent Cell Viability Assay Reagent (Promega: G7571) was added to the
595 duplicate plate, then incubated for 15 minutes at RT on an orbital shaker, then luminescence was recorded.
596 Difference in luminescence from baseline to the 48 hour timepoint was used as a proxy for changes in cell
597 viability.
598
599 **Apoptosis Assay**
600 This method refers to Figure S4H.
601 Cells were seeded in 6-well tissue culture dishes (Corning: 07-200-83) at 325K cells/well for 48H. Cell culture
602 media and wash media were collected and pooled with quenched trypsin-containing media containing cells and
603 apoptosis analysis was performed using an APC AnnexinV apoptosis detection kit (BioLegend, 640920)
604 according to the provided protocol. Flow cytometry was performed to quantify the percentage of annexin V^+ cells.
605
606 **Alkaline Comet Assay**
607 This method refers to Figure S4F
608 Comet assay 3-well slides (Cell Biolabs Cat# STA-353) were pre-coated with 1.5% medium-melting-point
609 agarose (Sigma Aldrich Cat#A6877-500g) and dried overnight. Harvested cells were resuspended in 0.5% low-
610 melting-point agarose (Lonza Cat#50101) at 37°C at 1 to 20 ratio. Cell suspension was spread onto pre-coated
611 slides and allowed to polymerize for 20 minutes in the dark. Then, slides were incubated in lysis buffer (10 mM
612 Tris-HCl, pH 10, 2.5 M NaCl, 0.1 M EDTA, 1% Triton X-100) for 30 minutes. Afterwards, samples were
613 incubated in alkaline running buffer (0.3 M NaOH, 1 mM EDTA) for 30 min before electrophoresed (300 mA, 20
614 V) for 15 min at 4°C. Slides were washed three times with distilled water (dH2O) and fixed with cold 70%
615 ethanol for 15 minutes. After completely drying the slides at 37 C, stain DNA on slides using 1 uM Yoyo-1

616 (Fisher Cat#3601) for 30 minutes in dark. Wash and dry stained slides overnight. Images acquired using the
617 Zeiss Axiocam 506 Mono.
618
619 **Immunoblotting**
620 This method refers to figures 1D, 1E, S1C-S1H, S1I, S2C, S2F, 4F-4H, S4G, S4I, 5H, S5E, S5I, 6A and S6D.
621 Cells were lysed in RIPA buffer (50 mM Tris-HCl pH 8.0, 150 nM NaCl, 1% NP-40, 0.5%Sodium Deoxycholate,
622 0.1% SDS) containing a phosphatase inhibitor cocktail (Halt: 78428) and a protease inhibitor cocktail (Millipore
623 Sigma: 1169749). Sonication was performed with a sonic dismembrator (ThermoFisher Scientific: FB120). For
624 isolation of protein from tumors, small portions were isolated using dissociation with a razor blade, then added
625 to RIPA lysis buffer in bead mill tubes (ThermoFisher Scientific: 15-340-164). The mixture was shaken 60
626 seconds 2x at max intensity using a Bead Mill 4 homogenizer (ThermoFisher Scientific: 15-340-164).
627 Protein concentration was calculated by the Pierce™ BCA Protein Assay (ThermoFisher Scientific: PI23228)
628 according to manufacturer specifications. Samples were run on NuPAGE 4-12% Bis-Tris Gels (ThermoFisher
629 Scientific: NP0335, NP0322) at 200V for 40-50 minutes, then transferred to Immobilon™-P PVDF Membranes
630 (Millipore Sigma: IPVH 00010) at 30V for 60 minutes. Total protein was visualized using the Sypro Ruby protein
631 blot stain (ThermoFisher Scientific: S11791).
632 Membranes were blocked in 5% Milk (LabScientific: M0841) in DPBS without calcium or magnesium (Gibco: 21-
633 600-044) with 0.1% Tween-20 (Fisher: BP337) for at least 1 hour at RT on an orbital shaker. Membranes were
634 then probed with primary antibodies overnight at 4°C, followed by chromophore-conjugated Alexa Fluor 647 anti-
635 mouse (ThermoFisher Scientific: A21235), Alexa Fluor 647 anti-rabbit (ThermoFisher Scientific: A21244), HRP-
636 conjugated anti-mouse (ThermoFisher Scientific: 31437), or anti-rabbit (ThermoFisher Scientific: G-21234)
637 secondary antibodies. Chromophore-conjugated antibodies were detected by fluorescence using a GE Typhoon
638 FLA 9000 Gel Imaging Scanner or Invitrogen IBright 1500. HRP-conjugated antibodies were detected using
639 chemiluminescent detection on film (Fisher: PI34091). Primary antibodies used were β-Actin (Invitrogen: PIMA-
640 1140), Prostate Specific Antigen (PSA) (Cell Signaling: 5877S), OGDHL (Invitrogen MA5-62626), OGDH
641 (Proteintech: 15212-1-AP), Phospho-Histone H2A.X(Ser 139) (γH2AX) (Cell Signaling: 9718S), Vinculin
642 (Abcam: ab129002), HES6 (NovusBio: NBP3-04548), and DLL3 (Cell Signaling: 71804S).
643

644 ***In vitro* RNA Sequencing**

645 This method refers to Figure 2A-E, S2A, S2B, S2D, S2E, 4B-4E, S4B-S4D, 5A-5D, S5A-S5D, 6F-6H, S6B and
646 S6C.

647 Cells were plated into 6-well tissue culture dishes (Corning: 07-200-83) at 325K cells/well. After 48 hours, cells
648 were lifted cell lines were detached from tissue culture plates using 0.05% Trypsin-EDTA, Phenol Red (Gibco:
649 25-300-120) at 37°C for 5 minutes then quenched with culture medium, then pelleted by centrifugation.
650 Supernatant was removed and cells were washed once with sterile DPBS without Calcium and Magnesium
651 (Gibco: 14-190-20), then the supernatant was removed, and cells were flash frozen using Liquid N_2. Cell pellets
652 were maintained at -80°C until submission for sequencing.

653

654 ***In vivo* RNA Sequencing**

655 This method refers to Figure 2F, 4A, S4A, 5E-5G, S5G, and S5H

656 Small tumor sections were isolated from harvested tumors and flash frozen using flash frozen using Liquid N_2.
657 Tumor sections were maintained at -80°C until submission for sequencing.

658 Libraries for RNA-Seq were prepared with KAPA mRNA HyperPrep Kit. The workflow consists of mRNA
659 enrichment and fragmentation, first strand cDNA synthesis using random priming followed by second strand
660 synthesis converting cDNA:RNA hybrid to double-stranded cDNA (dscDNA), and incorporates dUTP into the
661 second cDNA strand to maintain strand origin information. cDNA generation is followed by end repair to generate
662 blunt ends, A-tailing, adaptor ligation and PCR amplification. Different adaptors were used for multiplexing
663 samples in a half lane. Sequencing was performed on Illumina NovaSeq X Plus for PE 2x50 run. Data quality
664 check was done on Illumina SAV. Demultiplexing was performed with Illumina Bcl2fastq v2.19.1.403 software.

665 The alignment was performed using STAR[100] with human reference genome GRCh38. The Ensembl Transcripts
666 release GRCh38.107 GTF was used for gene feature annotation. For normalization of transcripts counts, TPM
667 normalized counts were generated.

668 **Confocal Microscopy**

669 This method refers to Figure 6B and 6C

670 Cells were plated onto sterilized glass coverslips in 24-well tissue culture dishes (Corning: 09-761-146) at 15K
671 cells/well. Once cells reached 80% confluency, media was removed and cells were washed with sterile PBS.
672 Cells were then fixed in 4% Paraformaldehyde in PBS for 20 minutes at RT. After fixation, cells were washed

673 with PBS, then permeabilized using 0.5% Triton X-100 in PBS for 5 minutes at 4°C, followed by 3 PBS washes.
674 Coverslips were then blocked with PBS containing 3% BSA and 0.1% Tween-20 for 30 minutes at RT, before
675 adding primary antibody for 1 Hour at RT in the dark. Following primary antibody staining, coverslips were
676 washed 3 times with PBS containing 0.1% Tween-20. Then fluorophore-conjugated secondary antibodies were
677 added for 1 hour at RT in the dark. Following secondary staining, coverslips were washed twice with PBS
678 containing 0.1% Tween-20. DAPI (1:2000) was added during a final wash in 0.1% Tween-20 for 5 minutes.
679 Coverslips were mounted onto glass slides using Prolong Gold (Thermofisher: P36930) and allowed to dry
680 overnight in the dark. Slides were sealed with clear nail polish until imaging. Imaging was completed using the
681 Zeiss LSM 980 Airyscan 2 using a 63X oil immersion objective. Primary Antibodies used were OGDHL
682 (Invitrogen MA5-62626) and TUFM (Atlas: AMAB909066), Secondary Antibodies used were anti-Rabbit IgG
683 Alexa Fluor 647 and anti-Mouse IgG Alexa Fluor 594.
684

685 **Differential gene expression models**

686 This method refers to Figure 7A

687 Differentially expressed gene (DEG) models were fit in R (v4.2.3)(R Core team) using the limma package
688 (v3.54.2) lmFit function[101]. Models were constructed using the log2-transformation of reads per kilobase of
689 transcript per million reads mapped (RPKM) plus one pseudo count as the outcome and an ordinal encoding of
690 genotype as the predictor for each gene independently as follows:

691 $$Y_i \approx \beta_{0i} + \beta_{1i}X$$

692 Here Y_i represents a sample outcome vector for an individual gene and β_{0i} represents the model intercept for
693 an individual gene. X represents the genotype vector, which is defined as a z-scored vector of integers
694 representing the varying genotypes in order of disease severity being experimentally modeled. β_{1i} represents
695 the multiplicative change (in doublings) in expression per standard deviation increase in genotypic sate for an
696 individual gene.

697 Standard errors were moderated using the limma eBayes function[101]. Estimate P-values were adjusted using the
698 Benjamini-Hochberg false discovery rate (FDR) procedure.

699 **RNA Alignment and Quality Control**

700 This method refers to Figure S7A-S7C.

701 RNA sequencing data, provided as FASTQ files, were obtained for multiple study cohorts (Long et al.,
702 NCT01990196, Sharma et al., Wilkinson et al.)[74–76]. All datasets were processed uniformly through metapipeline-
703 RNA (v1.0.0)[102]. Reads were aligned to the GRCh38.14 human reference genome using the STAR aligner
704 (v2.7.11a)[101]. Gene annotations were based on GENCODE Release 45[103]. Initial quality control (QC)
705 assessments for the raw sequencing reads were conducted using FastQC (v0.11.8), which evaluated metrics
706 such as per-base sequence quality, sequence content, and GC content. Post-alignment QC metrics were
707 generated by STAR, including error rates, read length distributions, splicing characteristics, and overall alignment
708 statistics (e.g., percentage of uniquely mapped reads). MultiQC (v1.25) was employed to aggregate and
709 summarize the QC metrics from both FastQC and STAR across all samples[104]. Samples identified as QC outliers
710 using a significance cutoff of 0.05 based on FastQC statistics were removed using OmicsQC[105]. Subsequently,
711 gene and transcript quantification was performed using RSEM (v1.3.3) based on the STAR alignments[106]

712

713 **Statistical Analysis of OGDHL Gene Expression in patients pre- and post- ADT Therapy**

714 Gene expression levels for *OGDHL* (Oxoglutarate Dehydrogenase L), quantified as Transcripts Per Million
715 (TPM), were used for differential expression analysis. Expression values were $\log_2$-transformed after adding a
716 pseudocount of 1 ($\log_2$(TPM + 1)) prior to statistical testing and visualization. Data from the individual cohorts
717 were aggregated for combined analyses where appropriate.

718 To compare *OGDHL* expression between 'Pre' and 'Post' conditions using all available samples irrespective of
719 pairing, a two-sided Wilcoxon rank-sum test was performed on the aggregated dataset (n=231 Pre, n=109 Post
720 samples; Fig. S7A).

721 For samples where paired data were available (i.e., measurements from the same individual under both 'Pre'
722 and 'Post' conditions, n=84 pairs), a two-sided Wilcoxon signed-rank test was employed to assess significant
723 changes in expression within individuals (Fig. S7B). In cases where multiple samples from one condition were
724 present within an individual, their average TPM was taken and considered as a single sample.

725 The $\log_2$ Fold Change ($\log_2$FC) was calculated for each study cohort and the combined dataset by comparing
726 the average $\log_2$(TPM + 1) expression in the 'Post' condition relative to the 'Pre' condition.

727 A summary dot plot was generated to visualize the differential expression results across studies (Fig. S6C). In
728 this plot, the size and color of the dots represent the calculated log_2FC. The statistical significance of the
729 comparison for each study (and the combined 'All' dataset), stratified by unpaired and paired analysis types, is
730 indicated by the background shading intensity. P-values obtained from the respective statistical tests (Wilcoxon
731 rank-sum for unpaired, Wilcoxon signed-rank for paired) were adjusted for multiple comparisons across the
732 studies shown using a Bonferroni correction. Darker shading corresponds to a lower adjusted P-value.

733 All statistical analyses and data visualizations were performed using R version (v4.3.3),
734 BoutrosLab.plotting.general (v7.1.2), data.table (v1.17.0), and cowplot (v1.1.2)[107–110].

735 **Statistical Analysis**

736 **Western Blot Quantification**

737 Relative expression was calculated by opening image files in FIJI then inverting to negative. Mean band intensity
738 was measured and plotted as a ratio of protein of interest/loading control. P-values were calculated using
739 unpaired t-tests with Welch's correction.

740 **Statistical analysis of tumor formation rate**

741 Equivalent volume of injection media was weighed as a baseline for input material. Tissue recovered after 4
742 weeks *in vivo* was weighed and compared to the injection media baseline. P-values for tumor formation was
743 calculated by a 2-tailed Fisher's Exact Test.

744 **Metabolomics Analysis**

745 Metabolite abundance and isotopologue distributions were calculated by normalizing to cell number. Metabolite
746 abundance was measured as the sum of all isotopologues. Fold changes were calculating by averaging
747 metabolite abundance values of control cells relative. False Discovery Rate (FDR) was calculated by applying
748 the Benjamini-Hochberg procedure for multiple hypothesis testing to p-values corresponding to 2-tailed t-tests.
749 Volcano plot was generated by plotting the log_2 transformed fold change and negative log_{10} transformed FDR
750 values. Heat maps were generated by plotting Row Z scores of metabolite abundance of knockdown cells or
751 control.

752 **RNA sequencing Analysis**

753 Fold changes in RNA expression were calculated by normalizing measured TPM values to the average of the
754 control group. False Discovery Rate (FDR) was calculated by applying the Benjamini-Hochberg procedure for
755 multiple hypothesis testing to p-values corresponding to 2-tailed t-tests. Heat maps were generated by plotting
756 fold change or $\log_2$ transformed fold change in TPM relative to control. Volcano plot was generated by plotting
757 the $\log_2$ transformed fold change and negative $\log_{10}$ transformed FDR values. Gene Set Enrichment Analysis
758 (GSEA) was performed using the Hallmark gene sets from the Molecular Signatures Database (MSigDB) using
759 GSEA (v 4.3.3)[111,112]. Gene sets were gathered from the MSigDB or specified source. Row Z scores were
760 calculated, then plotted as the average for the control or OGDHL knockdown/knockout condition.

761 Previously Published Data Sets

762 RNA-sequencing data sets were generated as previously described[67–73]. Bulk RNA-sequencing data that was
763 re-analyzed for this manuscript were obtained as normalized transcript values. Figures 6A and 6B were
764 generated from data published by Ku *et al.*[67]. Figure 6C was generated by NEPC patient tumor data published
765 by Beltran *et al.*[68]. Data for Figures 6D-6E were collected from the StandUp2Cancer mCRPC dataset[69], UW
766 Rapid Autopsy Data Set[71], and the LUCaP PDX Data Set[72], stratification of groups completed by Labraque *et*
767 *al.*[69]. Data for Circulating Tumor Cells obtained from Sharifi *et al.*[73] Statistical analysis was completed by unpaired
768 T-Test with Welch's correction.

769 **Immunofluorescence Quantification**

770 Mitochondrial colocalization analysis was completed by opening TUFM (mitochondrial) and OGDHL channels
771 using FIJI then measured by the Colocalization Function. OGDHL localization was calculated by measuring total
772 OGDHL Fluorescence intensity in FIJI, then subtracting out the Mitochondrial (TUFM) or Nuclear (DAPI) signal
773 regions using Region of Interest (ROI) Manager. Background values were removed by subtracting the Mean
774 Fluorescence observed in OGDHL knockout cells.

775

776

777 **Data Accessibility**

778 RNA-Sequencing files were uploaded to Gene Expression Omnibus:

779 Accension IDs: GSE298123, GSE297510, and GSE298381

780

Raw metabolomics data is is available at the NIH Common Fund's National Metabolomics Data Repository (NMDR) website, the Metabolomics Workbench[113], https://www.metabolomicsworkbench.org *where it has been assigned Project IDs 5929 and 5931.*

Acknowledgements

M.J.B. acknowledges the support of the Ruth L. Kirschstein National Research Service Award GM007185 and the NIDDK TL1 DK132768 Award. J.A.D. is supported by the Eugene V. Cota-Robles Fellowship. R.A. is supported by the UCLA-Caltech Medical Scientist Training Program T32GM152342 and the Jonsson Comprehensive Cancer Center Fellowship. S.L. is supported by the UCLA Jonsson Comprehensive Cancer Center. M.N.S is supported by the 2022 Point Biopharma Young Valor Investigator award and the Department of Defense PC220240. M.C.H. is supported by the NIH/NCI (R37CA286450), Grant 2021184 from the Doris Duke Charitable Foundation, the V Foundation, the Prostate Cancer Foundation Felix Feng PC-SYNERGY award and the UW/FHCC Institute for Prostate Cancer Research. D.B.S. is supported by NIH/NCI grants R01CA267721 and R01CA208642. P.C.B. is supported by the NIH grants P30CA016042, U2CCA271894, R01CA270108 and Department of Defense grants W81XWH2210247 and W81XWH2210751. A.S.G. is supported by UCLA Prostate Cancer Specialized Programs of Research Excellence (SPORE) NCI P50 CA092131, Department of Defense PCRP award HT94252310379, the Mike Slive Foundation for Prostate Cancer Research, the UC Cancer Research Coordinating Committee (C23CR5598), the 2024 Larry & Sherry Benaroya- Prostate Cancer Foundation Challenge Award, the Basser Center for BRCA, the UCLA Eli and Edythe Broad Center of Regenerative Medicine and Stem Cell Research Rose Hills Foundation Innovator Grant, the UCLA Jonsson Comprehensive Cancer Center and Eli and Edythe Broad Center of Regenerative Medicine and Stem Cell Research Ablon Scholars Program, the National Center for Advancing Translational Sciences UCLA CTSI Grant UL1TR001881, STOP CANCER, and the UCLA Institute of Urologic Oncology. The authors would like to thank Dr. Peter Nelson for LuCAP35CR cells and Dr. Nora Navone for MDA-PCa 180-30 patient derived xenograft tissue. We thank the UCLA metabolomics core and members of the Christofk lab for assistance with mass spectrometry and guidance in experimental design. We would also like to thank the UCLA Technology Center for Genomics & Bioinformatics (TCBG) for help with RNA sequencing and data analysis. *This work is supported by Metabolomics Workbench/National Metabolomics Data Repository (NMDR) (grant# U2C-DK119886), Common Fund Data Ecosystem (CFDE) (grant# 3OT2OD030544) and Metabolomics Consortium Coordinating Center (M3C) (grant# 1U2C-DK119889). Some figures were created using BioRender: Created in BioRender. Bernard, M. (2025)* https://BioRender.com/82da7ku. The funders had no role in study design, data collection and

822 analysis, decision to publish or preparation of the manuscript. We also thank Bill Lowry, Leigh Ellis, Hilary Coller,
823 and Brigitte Gomperts for providing critical feedback and intellectual support during the project.
824

825 **Author Contributions**
826
827 M.J.B., A.R., J.A.D., R.N.D., K.Y.H., S.B., A.G., E.L., S.Z., and T.H. conducted the experiments. M.J.B., N.M.N,
828 C.M.S., and R.A. completed data quantification and statistical analyses. M.J.B. and A.S.G. designed the
829 experiments, wrote, and edited the manuscript. B.R.W. performed molecular cloning and advised on genetic
830 knockout experiments. N.M. and H.R.C. provided metabolomics expertise, performed mass spectrometry on *in*
831 *vitro* nutrient tracing experiments, and wrote the related methods section. S.L. and D.B.S provided expertise
832 with PET experiments. N.M.N, R.A., H.M.R., M.C.H. and P.C.B. analyzed clinical data sets and provided
833 bioinformatics expertise. M.N.S., J.M.L., S.G.Z., analyzed and provided data corresponding to circulating tumor
834 cells. A.S.G. procured funding and supervised the project.
835

836 Competing interests: A.S.G. and D.B.S. are co-founders and consultants of Senergy Bio.

837 1. Finley, L. W. S. What is cancer metabolism? *Cell* **186**, 1670–1688 (2023).
838 2. Kinnaird, A., Zhao, S., Wellen, K. E. & Michelakis, E. D. Metabolic control of epigenetics in cancer. *Nat.*
839 *Rev. Cancer* **16**, 694–707 (2016).
840 3. Shapira, S. N. & Christofk, H. R. Metabolic Regulation of Tissue Stem Cells. *Trends Cell Biol.* **30**, 566–576
841 (2020).
842 4. DeBerardinis, R. J. & Chandel, N. S. Fundamentals of cancer metabolism. *Sci. Adv.* **2**, e1600200 (2016).
843 5. Faubert, B., Solmonson, A. & DeBerardinis, R. J. Metabolic reprogramming and cancer progression.
844 *Science* **368**, eaaw5473 (2020).
845 6. Wellen, K. E. & Thompson, C. B. A two-way street: reciprocal regulation of metabolism and signalling.
846 *Nat. Rev. Mol. Cell Biol.* **13**, 270–276 (2012).
847 7. Ghosh-Choudhary, S., Liu, J. & Finkel, T. Metabolic Regulation of Cell Fate and Function. *Trends Cell*
848 *Biol.* **30**, 201–212 (2020).
849 8. Morrison, A. J. Cancer cell metabolism connects epigenetic modifications to transcriptional regulation.
850 *FEBS J.* **289**, 1302–1314 (2022).
851 9. Yang, W. *et al.* ERK1/2-dependent phosphorylation and nuclear translocation of PKM2 promotes the
852 Warburg effect. *Nat. Cell Biol.* **14**, 1295–1304 (2012).
853 10. Sutendra, G. *et al.* A nuclear pyruvate dehydrogenase complex is important for the generation of acetyl-
854 CoA and histone acetylation. *Cell* **158**, 84–97 (2014).
855 11. Sharpley, M. S., Chi, F., Hoeve, J. T. & Banerjee, U. Metabolic plasticity drives development during
856 mammalian embryogenesis. *Dev. Cell* **56**, 2329-2347.e6 (2021).
857 12. Liu, X. *et al.* The existence of a nonclassical TCA cycle in the nucleus that wires the metabolic-epigenetic
858 circuitry. *Signal Transduct. Target. Ther.* **6**, 375 (2021).
859 13. Wang, L. *et al.* Prostate Cancer Incidence and Mortality: Global Status and Temporal Trends in 89
860 Countries From 2000 to 2019. *Front. Public Health* **10**, 811044 (2022).
861 14. Siegel, R. L., Kratzer, T. B., Giaquinto, A. N., Sung, H. & Jemal, A. Cancer statistics, 2025. *CA. Cancer J.*
862 *Clin.* **75**, 10–45 (2025).

863 15. Rebello, R. J. *et al.* Prostate cancer. *Nat. Rev. Dis. Primer* **7**, 9 (2021).
864 16. de Bono, J. S. *et al.* Abiraterone and increased survival in metastatic prostate cancer. *N. Engl. J. Med.* **364**,
865 1995–2005 (2011).
866 17. Scher, H. I. *et al.* Increased survival with enzalutamide in prostate cancer after chemotherapy. *N. Engl. J.*
867 *Med.* **367**, 1187–1197 (2012).
868 18. Beltran, H. *et al.* The Role of Lineage Plasticity in Prostate Cancer Therapy Resistance. *Clin. Cancer Res.*
869 *Off. J. Am. Assoc. Cancer Res.* **25**, 6916–6924 (2019).
870 19. Abida, W., Beltran, H. & Raychaudhuri, R. State of the Art: Personalizing Treatment for Patients With
871 Metastatic Castration-Resistant Prostate Cancer. *Am. Soc. Clin. Oncol. Educ. Book Am. Soc. Clin. Oncol.*
872 *Annu. Meet.* **45**, e473636 (2025).
873 20. Sayegh, N., Swami, U. & Agarwal, N. Recent Advances in the Management of Metastatic Prostate Cancer.
874 *JCO Oncol. Pract.* **18**, 45–55 (2022).
875 21. Crowell, P. D. *et al.* MYC is a regulator of androgen receptor inhibition-induced metabolic requirements in
876 prostate cancer. *Cell Rep.* **42**, 113221 (2023).
877 22. Reina-Campos, M. *et al.* Increased Serine and One-Carbon Pathway Metabolism by PKCλ/ι Deficiency
878 Promotes Neuroendocrine Prostate Cancer. *Cancer Cell* **35**, 385-400.e9 (2019).
879 23. Labbé, D. P. *et al.* High-fat diet fuels prostate cancer progression by rewiring the metabolome and
880 amplifying the MYC program. *Nat. Commun.* **10**, 4358 (2019).
881 24. Basu, H. S. *et al.* Prostate cancer cells survive anti-androgen and mitochondrial metabolic inhibitors by
882 modulating glycolysis and mitochondrial metabolic activities. *The Prostate* **81**, 799–811 (2021).
883 25. Singh, R. & Mills, I. G. The Interplay Between Prostate Cancer Genomics, Metabolism, and the
884 Epigenome: Perspectives and Future Prospects. *Front. Oncol.* **11**, 704353 (2021).
885 26. Ahmad, F., Cherukuri, M. K. & Choyke, P. L. Metabolic reprogramming in prostate cancer. *Br. J. Cancer*
886 **125**, 1185–1196 (2021).
887 27. Intlekofer, A. M. & Finley, L. W. S. Metabolic signatures of cancer cells and stem cells. *Nat. Metab.* **1**,
888 177–188 (2019).

889 28. Bunik, V., Kaehne, T., Degtyarev, D., Shcherbakova, T. & Reiser, G. Novel isoenzyme of 2-oxoglutarate
890 dehydrogenase is identified in brain, but not in heart. *FEBS J.* **275**, 4990–5006 (2008).
891 29. Zhong, Y. *et al.* Structural basis for the activity and regulation of human α-ketoglutarate dehydrogenase
892 revealed by Cryo-EM. *Biochem. Biophys. Res. Commun.* **602**, 120–126 (2022).
893 30. Sen, T. *et al.* OGDHL is a modifier of AKT-dependent signaling and NF-κB function. *PloS One* **7**, e48770
894 (2012).
895 31. Liu, Y. *et al.* A Novel Oxoglutarate Dehydrogenase-Like Mediated miR-214/TWIST1 Negative Feedback
896 Loop Inhibits Pancreatic Cancer Growth and Metastasis. *Clin. Cancer Res. Off. J. Am. Assoc. Cancer Res.*
897 **25**, 5407–5421 (2019).
898 32. Dai, W. *et al.* OGDHL silencing promotes hepatocellular carcinoma by reprogramming glutamine
899 metabolism. *J. Hepatol.* **72**, 909–923 (2020).
900 33. Dai, W. *et al.* Silencing of OGDHL promotes liver cancer metastasis by enhancing hypoxia inducible factor
901 1 α protein stability. *Cancer Sci.* **114**, 1309–1323 (2023).
902 34. Shi, J. *et al.* The m6A modification-mediated OGDHL exerts a tumor suppressor role in ccRCC by
903 downregulating FASN to inhibit lipid synthesis and ERK signaling. *Cell Death Dis.* **14**, 560 (2023).
904 35. Jiang, X. *et al.* Oxoglutarate dehydrogenase-like inhibits the progression of hepatocellular carcinoma by
905 inducing DNA damage through non-canonical function. *Cell Death Differ.* **30**, 1931–1942 (2023).
906 36. Roy, R., Chun, J. & Powell, S. N. BRCA1 and BRCA2: different roles in a common pathway of genome
907 protection. *Nat. Rev. Cancer* **12**, 68–78 (2011).
908 37. Mantovani, F., Collavin, L. & Del Sal, G. Mutant p53 as a guardian of the cancer cell. *Cell Death Differ.*
909 **26**, 199–212 (2019).
910 38. Engeland, K. Cell cycle regulation: p53-p21-RB signaling. *Cell Death Differ.* **29**, 946–960 (2022).
911 39. Hanahan, D. & Weinberg, R. A. Hallmarks of cancer: the next generation. *Cell* **144**, 646–674 (2011).
912 40. Lane, A. N. & Fan, T. W.-M. Regulation of mammalian nucleotide metabolism and biosynthesis. *Nucleic*
913 *Acids Res.* **43**, 2466–2485 (2015).

914 41. Villa, E., Ali, E. S., Sahu, U. & Ben-Sahra, I. Cancer Cells Tune the Signaling Pathways to Empower de
915 Novo Synthesis of Nucleotides. *Cancers* **11**, 688 (2019).
916 42. Palanisamy, N. *et al.* The MD Anderson Prostate Cancer Patient-derived Xenograft Series (MDA PCa
917 PDX) Captures the Molecular Landscape of Prostate Cancer and Facilitates Marker-driven Therapy
918 Development. *Clin. Cancer Res. Off. J. Am. Assoc. Cancer Res.* **26**, 4933–4946 (2020).
919 43. Jiao, Y. *et al.* OGDHL Expression as a Prognostic Biomarker for Liver Cancer Patients. *Dis. Markers* **2019**,
920 9037131 (2019).
921 44. Mao, M. *et al.* OGDHL closely associates with tumor microenvironment and can serve as a prognostic
922 biomarker for papillary thyroid cancer. *Cancer Med.* **10**, 728–736 (2021).
923 45. Bunik, V. I., Romash, O. G. & Gomazkova, V. S. Effect of alpha-ketoglutarate and its structural analogues
924 on hysteretic properties of alpha-ketoglutarate dehydrogenase. *FEBS Lett.* **278**, 147–150 (1991).
925 46. Diehl, F. F. *et al.* Nucleotide imbalance decouples cell growth from cell proliferation. *Nat. Cell Biol.* **24**,
926 1252–1264 (2022).
927 47. Bester, A. C. *et al.* Nucleotide deficiency promotes genomic instability in early stages of cancer
928 development. *Cell* **145**, 435–446 (2011).
929 48. Zeman, M. K. & Cimprich, K. A. Causes and consequences of replication stress. *Nat. Cell Biol.* **16**, 2–9
930 (2014).
931 49. Challis, D. *et al.* Multiomics analysis of adaptation to repeated DNA damage in prostate cancer cells.
932 *Epigenetics* **18**, 2214047 (2023).
933 50. Mah, L.-J., El-Osta, A. & Karagiannis, T. C. gammaH2AX: a sensitive molecular marker of DNA damage
934 and repair. *Leukemia* **24**, 679–686 (2010).
935 51. Hirano, D., Okada, Y., Minei, S., Takimoto, Y. & Nemoto, N. Neuroendocrine differentiation in hormone
936 refractory prostate cancer following androgen deprivation therapy. *Eur. Urol.* **45**, 586–592; discussion 592
937 (2004).
938 52. Sherman, M. H., Bassing, C. H. & Teitell, M. A. Regulation of cell differentiation by the DNA damage
939 response. *Trends Cell Biol.* **21**, 312–319 (2011).

940 53. Do, B. T. *et al.* Nucleotide depletion promotes cell fate transitions by inducing DNA replication stress. *Dev.*
941 *Cell* **59**, 2203-2221.e15 (2024).
942 54. Nouri, M. *et al.* Transient Sox9 Expression Facilitates Resistance to Androgen-Targeted Therapy in Prostate
943 Cancer. *Clin. Cancer Res. Off. J. Am. Assoc. Cancer Res.* **26**, 1678–1689 (2020).
944 55. Bae, S., Bessho, Y., Hojo, M. & Kageyama, R. The bHLH gene Hes6, an inhibitor of Hes1, promotes
945 neuronal differentiation. *Dev. Camb. Engl.* **127**, 2933–2943 (2000).
946 56. Koyano-Nakagawa, N., Kim, J., Anderson, D. & Kintner, C. Hes6 acts in a positive feedback loop with the
947 neurogenins to promote neuronal differentiation. *Dev. Camb. Engl.* **127**, 4203–4216 (2000).
948 57. Gratton, M.-O. *et al.* Hes6 promotes cortical neurogenesis and inhibits Hes1 transcription repression activity
949 by multiple mechanisms. *Mol. Cell. Biol.* **23**, 6922–6935 (2003).
950 58. Vias, M. *et al.* Pro-neural transcription factors as cancer markers. *BMC Med. Genomics* **1**, 17 (2008).
951 59. Qi, J. *et al.* Siah2-dependent concerted activity of HIF and FoxA2 regulates formation of neuroendocrine
952 phenotype and neuroendocrine prostate tumors. *Cancer Cell* **18**, 23–38 (2010).
953 60. Carvalho, F. L. F. *et al.* HES6 promotes prostate cancer aggressiveness independently of Notch signalling.
954 *J. Cell. Mol. Med.* **19**, 1624–1636 (2015).
955 61. Annala, M. *et al.* DOT1L-HES6 fusion drives androgen independent growth in prostate cancer. *EMBO Mol.*
956 *Med.* **6**, 1121–1123 (2014).
957 62. Wang, Y. *et al.* Deciphering the Transcription Factor Landscape in Prostate Cancer Progression: A Novel
958 Approach to Understand NE Transdifferentiation. *Adv. Sci. Weinh. Baden-Wurtt. Ger.* **12**, e2404938 (2025).
959 63. Ramos-Montoya, A. *et al.* HES6 drives a critical AR transcriptional programme to induce castration-
960 resistant prostate cancer through activation of an E2F1-mediated cell cycle network. *EMBO Mol. Med.* **6**,
961 651–661 (2014).
962 64. Wang, Y. *et al.* KAT2A coupled with the α-KGDH complex acts as a histone H3 succinyltransferase.
963 *Nature* **552**, 273–277 (2017).
964 65. Nagaraj, R. *et al.* Nuclear Localization of Mitochondrial TCA Cycle Enzymes as a Critical Step in
965 Mammalian Zygotic Genome Activation. *Cell* **168**, 210-223.e11 (2017).

966 66. Sivanand, S. *et al.* Nuclear Acetyl-CoA Production by ACLY Promotes Homologous Recombination. *Mol.*
967 *Cell* **67**, 252-265.e6 (2017).
968 67. Ku, S. Y. *et al.* Rb1 and Trp53 cooperate to suppress prostate cancer lineage plasticity, metastasis, and
969 antiandrogen resistance. *Science* **355**, 78–83 (2017).
970 68. Beltran, H. *et al.* Divergent clonal evolution of castration-resistant neuroendocrine prostate cancer. *Nat.*
971 *Med.* **22**, 298–305 (2016).
972 69. Labrecque, M. P. *et al.* Molecular profiling stratifies diverse phenotypes of treatment-refractory metastatic
973 castration-resistant prostate cancer. *J. Clin. Invest.* **129**, 4492–4505 (2019).
974 70. Robinson, D. *et al.* Integrative clinical genomics of advanced prostate cancer. *Cell* **161**, 1215–1228 (2015).
975 71. Morrissey, C. *et al.* Effects of androgen deprivation therapy and bisphosphonate treatment on bone in
976 patients with metastatic castration-resistant prostate cancer: results from the University of Washington
977 Rapid Autopsy Series. *J. Bone Miner. Res. Off. J. Am. Soc. Bone Miner. Res.* **28**, 333–340 (2013).
978 72. Nguyen, H. M. *et al.* LuCaP Prostate Cancer Patient-Derived Xenografts Reflect the Molecular
979 Heterogeneity of Advanced Disease an--d Serve as Models for Evaluating Cancer Therapeutics. *The*
980 *Prostate* **77**, 654–671 (2017).
981 73. Sharifi, M. N. *et al.* High-purity CTC RNA sequencing identifies prostate cancer lineage phenotypes
982 prognostic for clinical outcomes. *Cancer Discov.* (2025) doi:10.1158/2159-8290.CD-24-1509.
983 74. Long, X. *et al.* Immune signature driven by ADT-induced immune microenvironment remodeling in
984 prostate cancer is correlated with recurrence-free survival and immune infiltration. *Cell Death Dis.* **11**, 779
985 (2020).
986 75. Sharma, N. V. *et al.* Identification of the Transcription Factor Relationships Associated with Androgen
987 Deprivation Therapy Response and Metastatic Progression in Prostate Cancer. *Cancers* **10**, 379 (2018).
988 76. Wilkinson, S. *et al.* Nascent Prostate Cancer Heterogeneity Drives Evolution and Resistance to Intense
989 Hormonal Therapy. *Eur. Urol.* **80**, 746–757 (2021).
990 77. Koppens, M. & van Lohuizen, M. Context-dependent actions of Polycomb repressors in cancer. *Oncogene*
991 **35**, 1341–1352 (2016).

992 78. Cao, J. *et al.* Histone demethylase RBP2 is critical for breast cancer progression and metastasis. *Cell Rep.* **6**,
993 868–877 (2014).
994 79. Teng, Y.-C. *et al.* Histone demethylase RBP2 promotes lung tumorigenesis and cancer metastasis. *Cancer*
995 *Res.* **73**, 4711–4721 (2013).
996 80. Ikushima, H. & Miyazono, K. Cellular context-dependent 'colors' of transforming growth factor-beta
997 signaling. *Cancer Sci.* **101**, 306–312 (2010).
998 81. Golias, T. *et al.* Hypoxic repression of pyruvate dehydrogenase activity is necessary for metabolic
999 reprogramming and growth of model tumours. *Sci. Rep.* **6**, 31146 (2016).
000 82. Liu, Z. *et al.* miR-21-5p targets PDHA1 to regulate glycolysis and cancer progression in gastric cancer.
001 *Oncol. Rep.* **40**, 2955–2963 (2018).
002 83. Penugurti, V., Mishra, Y. G. & Manavathi, B. AMPK: An odyssey of a metabolic regulator, a tumor
003 suppressor, and now a contextual oncogene. *Biochim. Biophys. Acta Rev. Cancer* **1877**, 188785 (2022).
004 84. Li, X. *et al.* Nucleus-Translocated ACSS2 Promotes Gene Transcription for Lysosomal Biogenesis and
005 Autophagy. *Mol. Cell* **66**, 684-697.e9 (2017).
006 85. Guertin, D. A. & Wellen, K. E. Acetyl-CoA metabolism in cancer. *Nat. Rev. Cancer* **23**, 156–172 (2023).
007 86. Baksh, S. C. & Finley, L. W. S. Metabolic Coordination of Cell Fate by α-Ketoglutarate-Dependent
008 Dioxygenases. *Trends Cell Biol.* **31**, 24–36 (2021).
009 87. Jing, Y. *et al.* Semisynthesis of site-specifically succinylated histone reveals that succinylation regulates
010 nucleosome unwrapping rate and DNA accessibility. *Nucleic Acids Res.* **48**, 9538–9549 (2020).
011 88. Poli, J. *et al.* dNTP pools determine fork progression and origin usage under replication stress. *EMBO J.* **31**,
012 883–894 (2012).
013 89. Shi, D. D., Savani, M. R., Abdullah, K. G. & McBrayer, S. K. Emerging roles of nucleotide metabolism in
014 cancer. *Trends Cancer* **9**, 624–635 (2023).
015 90. Wu, H. *et al.* Targeting nucleotide metabolism: a promising approach to enhance cancer immunotherapy. *J.*
016 *Hematol. Oncol.J Hematol Oncol* **15**, 45 (2022).

017 91. Zhou, W. *et al.* Purine metabolism regulates DNA repair and therapy resistance in glioblastoma. *Nat.*
018 *Commun.* **11**, 3811 (2020).
019 92. Zou, S. *et al.* CSN6 Mediates Nucleotide Metabolism to Promote Tumor Development and
020 Chemoresistance in Colorectal Cancer. *Cancer Res.* **83**, 414–427 (2023).
021 93. Mullen, N. J. & Singh, P. K. Nucleotide metabolism: a pan-cancer metabolic dependency. *Nat. Rev. Cancer*
022 **23**, 275–294 (2023).
023 94. Crowell, P. D., Giafaglione, J. M., Hashimoto, T., Diaz, J. A. & Goldstein, A. S. Evaluating the
024 Differentiation Capacity of Mouse Prostate Epithelial Cells Using Organoid Culture. *J. Vis. Exp. JoVE*
025 (2019) doi:10.3791/60223.
026 95. Drost, J. *et al.* Organoid culture systems for prostate epithelial and cancer tissue. *Nat. Protoc.* **11**, 347–358
027 (2016).
028 96. Chambers, M. C. *et al.* A cross-platform toolkit for mass spectrometry and proteomics. *Nat. Biotechnol.* **30**,
029 918–920 (2012).
030 97. Pluskal, T., Castillo, S., Villar-Briones, A. & Oresic, M. MZmine 2: modular framework for processing,
031 visualizing, and analyzing mass spectrometry-based molecular profile data. *BMC Bioinformatics* **11**, 395
032 (2010).
033 98. Myers, O. D., Sumner, S. J., Li, S., Barnes, S. & Du, X. One Step Forward for Reducing False Positive and
034 False Negative Compound Identifications from Mass Spectrometry Metabolomics Data: New Algorithms
035 for Constructing Extracted Ion Chromatograms and Detecting Chromatographic Peaks. *Anal. Chem.* **89**,
036 8696–8703 (2017).
037 99. Su, X., Lu, W. & Rabinowitz, J. D. Metabolite Spectral Accuracy on Orbitraps. *Anal. Chem.* **89**, 5940–5948
038 (2017).
039 100. Dobin, A. *et al.* STAR: ultrafast universal RNA-seq aligner. *Bioinforma. Oxf. Engl.* **29**, 15–21 (2013).
040 101. Smyth, G. K. Linear models and empirical bayes methods for assessing differential expression in
041 microarray experiments. *Stat. Appl. Genet. Mol. Biol.* **3**, Article3 (2004).

042 102. Tebon, P. J. *et al.* Drug screening at single-organoid resolution via bioprinting and interferometry. *Nat.*
043 *Commun.* **14**, 3168 (2023).
044 103. Mudge, J. M. *et al.* GENCODE 2025: reference gene annotation for human and mouse. *Nucleic Acids*
045 *Res.* **53**, D966–D975 (2025).
046 104. Ewels, P., Magnusson, M., Lundin, S. & Käller, M. MultiQC: summarize analysis results for multiple
047 tools and samples in a single report. *Bioinforma. Oxf. Engl.* **32**, 3047–3048 (2016).
048 105. Frelin, A. H., Zhu, H. & Boutros, P. C. OmicsQC: Nominating Qality Control Outliers in Genomic
049 Profiling Studies. (2024).
050 106. Li, B. & Dewey, C. N. RSEM: accurate transcript quantification from RNA-Seq data with or without a
051 reference genome. *BMC Bioinformatics* **12**, 323 (2011).
052 107. Wilke, C. O. cowplot: Streamlined Plot Theme and Plot Annotations for "ggplot2." (2024).
053 108. Barrett, T. *et al.* data.table: Extension of "data.frame." (2025).
054 109. Boutros, P. C., P'ng, C., Green, J. & Prokopec, S. BoutrosLab.plotting.general: Functions to Create
055 Publication-Quality Plots. (2024).
056 110. R: The R Project for Statistical Computing.
057 111. Mootha, V. K. *et al.* PGC-1alpha-responsive genes involved in oxidative phosphorylation are
058 coordinately downregulated in human diabetes. *Nat. Genet.* **34**, 267–273 (2003).
059 112. Subramanian, A. *et al.* Gene set enrichment analysis: a knowledge-based approach for interpreting
060 genome-wide expression profiles. *Proc. Natl. Acad. Sci. U. S. A.* **102**, 15545–15550 (2005).
061 113. Sud, M. *et al.* Metabolomics Workbench: An international repository for metabolomics data and
062 metadata, metabolite standards, protocols, tutorials and training, and analysis tools. *Nucleic Acids Res.* **44**,
063 D463-470 (2016).

064

065
066

067

068 **Figure Legends**

069

070 **Figure 1: OGDHL supports proliferation of Enzalutamide-resistant prostate cancer cells *in vitro* and *in***
071 ***vivo***

072 **(A and B)** ^{18}F-FDG PET signal **(A)** or ^{18}F-BnTP PET signal **(B)** in MDA PCa 180-30 CRPC tumors treated with
073 Enza or Vehicle for 14 Days. **(C)** RNA expression of Canonical TCA cycle genes in Enza-Resistant (Enza^{R})
074 16D Cells relative to Enza-naïve cells. **(D)** Western Blot of changes in OGDHL, PSA and OGDH in response to
075 acquisition of Enza-resistance in 16D^{CRPC} cells. **(E and F)** Western Blot of elevated OGDHL expression in MDA
076 PCa 180-30 derived xenografts **(E)**, and quantification of *in vivo* western blot **(F)**. **(G)** Relative change in cell
077 viability over 48 hours with OGDHL overexpression. Plotted as change in viability relative to control cells. Data
078 from 5 (16D, LNCaP) or 6 (PC3) technical replicates. **(H)** Relative change in cell viability over 48 hours with
079 shRNA-mediated knockdown of OGDHL in Enza-Maintained 16D cells. Plotted as change in viability relative to
080 control. Data from 3 biological replicate experiments with 5 technical replicates each. **(I)** Measured tumoroid
081 diameter of Enza-maintained 16D cells after 2 weeks of 3D culture. Data from 3 biological replicate
082 experiments, >50 tumoroids measured per replicate. **(J)** Representative images of control (shScrambled) and
083 OGDHL knockdown (shOGDHL) tumoroids generated from Enza-Maintained 16D Cells. Scale Bar = 50 µm. **(K**
084 **and L)** Image of tissues recovered 4 weeks after implantation *in vivo* from Enza-maintained 16D^{CRPC} cells with
085 control (Scrambled) or OGDHL knockdown. Scale Bar = 1.0 cm. **(K)** Measured weights of tissues recovered 4
086 weeks after implantation *in vivo* from Enza-maintained 16D Cells with control (Scrambled) or OGDHL
087 knockdown **(L)**. Error bars represent +/- SEM. P-value calculated by unpaired t-test with Welch's Correction.

088

089 **Figure 2: Loss of OGDHL in CRPC cells alters transcription of cell stress and cell cycle associated**
090 **pathways *in vitro* and *in vivo***

091 **(A)** RNA expression of Canonical TCA cycle genes in OGDHL knockdown Enza-maintained 16D^{CRPC} cells *in*
092 *vitro* normalized to control knockdown values. Data represented as 3 technical replicates each from 2 shRNAs.
093 **(B)** Volcano Plot of Differentially Expressed Genes in shOGDHL Enza-maintained 16D^{CRPC} cells relative to
094 control. Color indicates FDR < 0.05 **(C)** Heatmap of isolated proliferation and cell stress genes in control and
095 OGDHL knockdown cells, with technical replicates shown. **(D-F)** Average expression of genes in Hallmark:

096 G2M Checkpoint, E2F Targets, and Myc Targets v1 with Enza-Maintained $16D^{CRPC}$ cells with acute knockdown
097 of OGDHL *in vitro* **(D)**, in OGDHL CRISPR knockout cell lines *in vitro* **(E)**, and in tumors formed from OGDHL
098 knockout cells **(F)**. Data shown is average Z scores from 3 control replicates and 6 knockdown/knockout
099 replicates *in vitro* or 5 control and 4 knockout replicates *in vivo.* Error bars represent +/- SEM. Adjusted P
100 values were calculated by applying the Benjamini-Hochberg procedure for multiple hypothesis testing to p-
101 values corresponding to 2-tailed t-tests.
102
103 **Figure 3: OGDHL loss perturbs nucleotide pools and glucose incorporation into nucleotides**
104 **(A)** Schematic of heavy-isotope (U-^{13}C Glucose or U-^{13}C Glutamine) nutrient tracing into TCA cycle and
105 nucleotide metabolic intermediates. **(B)** M + 2 labeled α-ketoglutarate from U-^{13}C glucose in control or OGDHL
106 knockdown Enza-maintained $16D^{CRPC}$ cells. Data represent 3 technical replicate experiments for each of 2
107 shRNAs. **(C)** Volcano Plot of differentially abundant metabolites from metabolic profiling of Enza-maintained
108 $16D^{CRPC}$ cells with OGDHL or control knockdown. Highlighted metabolites are nucleotide synthesis
109 intermediates. Line indicates FDR = 0.05. **(D)** Heatmap of nucleotide phosphate abundance in OGDHL
110 knockdown and control knockdown Enza-maintained $16D^{CRPC}$ cells. Data represented as row z scores from 3
111 technical replicates from each of 3 biological replicate lines. **(E and F)** Relative abundance of nucleotide
112 synthesis intermediates Phosphoribosyl pyrophosphate (PRPP) **(E)** and Dihydroorotate **(F)** from metabolic
113 profiling in control and OGDHL knockdown Enza-maintained $16D^{CRPC}$ cells. Data from 2 biological replicate
114 experiments (PRPP) or 3 biological replicates (Dihydroorotate) each with 3 technical replicates. **(G)** M + 5
115 labeling of pyrimidine phosphates derived from U-^{13}C glucose in control and OGDHL knockdown Enza-
116 maintained $16D^{CRPC}$ cells. Error bars represent +/- SEM. Adjusted P values were calculated by applying the
117 Benjamini-Hochberg procedure for multiple hypothesis testing to p-values corresponding to 2-tailed t-tests.
118
119 **Figure 4: OGDHL Loss reduces nucleotide synthesis gene expression and induces DNA damage *in***
120 ***vitro* and *in vivo***
121 **(A and B)** Relative RNA abundance of nucleotide synthesis genes in tumors formed from $16D^{CRPC}$ cells with
122 genetic knockout of OGDHL (n =4) or a control (n = 5) **(A)** or OGDHL knockout cells grown *in vitro* **(B).** Data
123 from 3 technical replicates each from 2 gRNAs. **(C)** Average Expression of genes in the KEGG: Pyrimidine

124 metabolism gene set in 16D^{CRPC} cells with genetic knockout of OGDHL. Data shown is average Z scores from
125 3 control replicates and 6 knockout replicates *in vitro.* **(D and E)** Average expression of genes in the Hallmark:
126 Apoptosis **(D)** and Hallmark: DNA Repair **(E)** gene sets with acute knockdown of OGDHL. Data shown is
127 average Z scores from 3 control replicates and 6 knockdown replicates *in vitro.* **(F-H)** Western blot of the DNA
128 damage marker γH2AX and OGDHL expression in control and OGDHL knockdown cells *in vitro* **(F)**, in cells
129 recovered 4 days after implantation *in vivo* **(G)** and in cells recovered 4 weeks after implantation *in vivo* **(H).**
130 Error bars represent +/- SEM. Adjusted P values were calculated by applying the Benjamini-Hochberg
131 procedure for multiple hypothesis testing to p-values corresponding to 2-tailed t-tests.
132
133 **Figure 5: OGDHL mediates lineage plasticity phenotypes and NE marker expression in prostate cancer**
134 **(A-C)** Average expression of genes in Gene Ontology Biological Pathway Gene Set: Axon Guidance **(A)**,
135 Hallmark: Epithelial Mesenchymal Transition (**B)** and Hallmark: Androgen Response **(C)** gene sets in 16D^{CRPC}
136 cells with CRISPR-Cas9 mediated genetic knockout of OGDHL allowed to adapt to enzalutamide for 6 weeks
137 *in vitro.* Data shown is average Z scores from 3 control replicates (+/- Enza) and 6 knockout replicates (+Enza)
138 *in vitro.* **(D)** mRNA expression of NEPC gene *HES6* in 16D^{CRPC} cells with genetic knockout of OGDHL cultured
139 *in vitro.* **(E and F)** mRNA expression of NEPC genes *HES6* **(E)** and *DLL3* **(F)** in tumors formed from 16D^{CRPC}
140 cells with genetic knockout of OGDHL (n =4) or control cells (n = 5). **(G)** Average expression of HES6 target
141 genes in tumors formed from 16D^{CRPC} cells with genetic knockout of OGDHL (n =4) or control (n = 5). **(H)**
142 Western blot of DLL3 and HES6 in control and OGDHL knockdown cell lines cells recovered 4 days after
143 implantation *in vivo*. Error bars represent +/- SEM. P-value calculated by unpaired t-test with Welch's
144 Correction.
145
146 **Figure 6: Mitochondrial localization of OGDHL is not required to regulate lineage and nucleotide**
147 **phenotypes**
148 **(A)** Schematic of CRISPR-resistant Full Length (FL) and mitochondrial targeting sequence deletion (ΔMTS)
149 OGDHL variants and validation of protein expression. **(B)** Immunofluorescence validation of OGDHL
150 subcellular localization in 16D^{CRPC} cells with CRISPR-Cas9 mediated genetic knockout of OGDHL and
151 expression of knockout-resistant FL and ΔMTS variants**. (C)** Representative image of subcellular localization of

endogenous OGDHL in enza-maintained $16D^{CRPC}$ cells. **(D and E)** Quantification of mitochondrial **(D)** and nuclear **(E)** localization of OGDHL. Data represented as % of OGDHL signal overlapping with the mitochondrial marker TUFM **(D)** or the nuclear stain DAPI **(E)**. Each data point represents a single cell. **(F-H)** Average expression of genes in the KEGG: Pyrimidine Metabolism **(F)** and HES6 Target Gene Set **(G)** and Hallmark: Myc Targets v1 **(H)** gene sets in $16D^{CRPC}$ cells with CRISPR-Cas9 mediated genetic knockout of OGDHL or reintroduction of knockout-resistant FL and ΔMTS variants. Data show average Z scores or TPM values from 3 technical replicates each. **(I)** M + 5 labeling of Uridine phosphates derived from U-^{13}C glucose in enza-maintained $16D^{CRPC}$ cells with genetic knockdown of OGDHL and expression of knockdown-resistant FL and ΔMTS variants. Data represent 3 technical replicates each**.** Error bars represent +/- SEM. P-value calculated by unpaired t-test with Welch's Correction.

Figure 7: OGDHL expression is elevated in Neuroendocrine Prostate Cancer

(A) Volcano plot of differentially expressed genes correlated with disease progression in the Ku *et al.* GEMM data set. Highlighted genes correspond to an FDR < 0.05. Names of the top 10 differentially regulated TCA cycle genes are displayed. (**B and C)** *OGDHL* mRNA expression in a GEMM model **(B)** of prostate adenocarcinoma (pten-null (SKO)) (n=4) and NEPC (pten;Rb1;TP53-null (TKO)) (n = 6) or in patients **(C)** with Adenocarcinoma (CRPC-Adeno) or NEPC (From Beltran *et al.*). **(D-F)** *OGDHL* mRNA in clinical metastatic CRPC specimens[70] **(D),** surgically resected tissue from patients who died from metastatic CRPC[71] **(E)**, and in Patient Derived Xenograft models of CRPC[72] based on AR expression and NE features[69,70]. **(G)** *OGDHL* mRNA expression in Circulating Tumor Cells (CTCs) from metastatic CRPC based on profiled subtype from the Sharifi *et al.* dataset[73.] Error bars represent +/- SEM. P-value calculated by unpaired t-test with Welch's Correction.

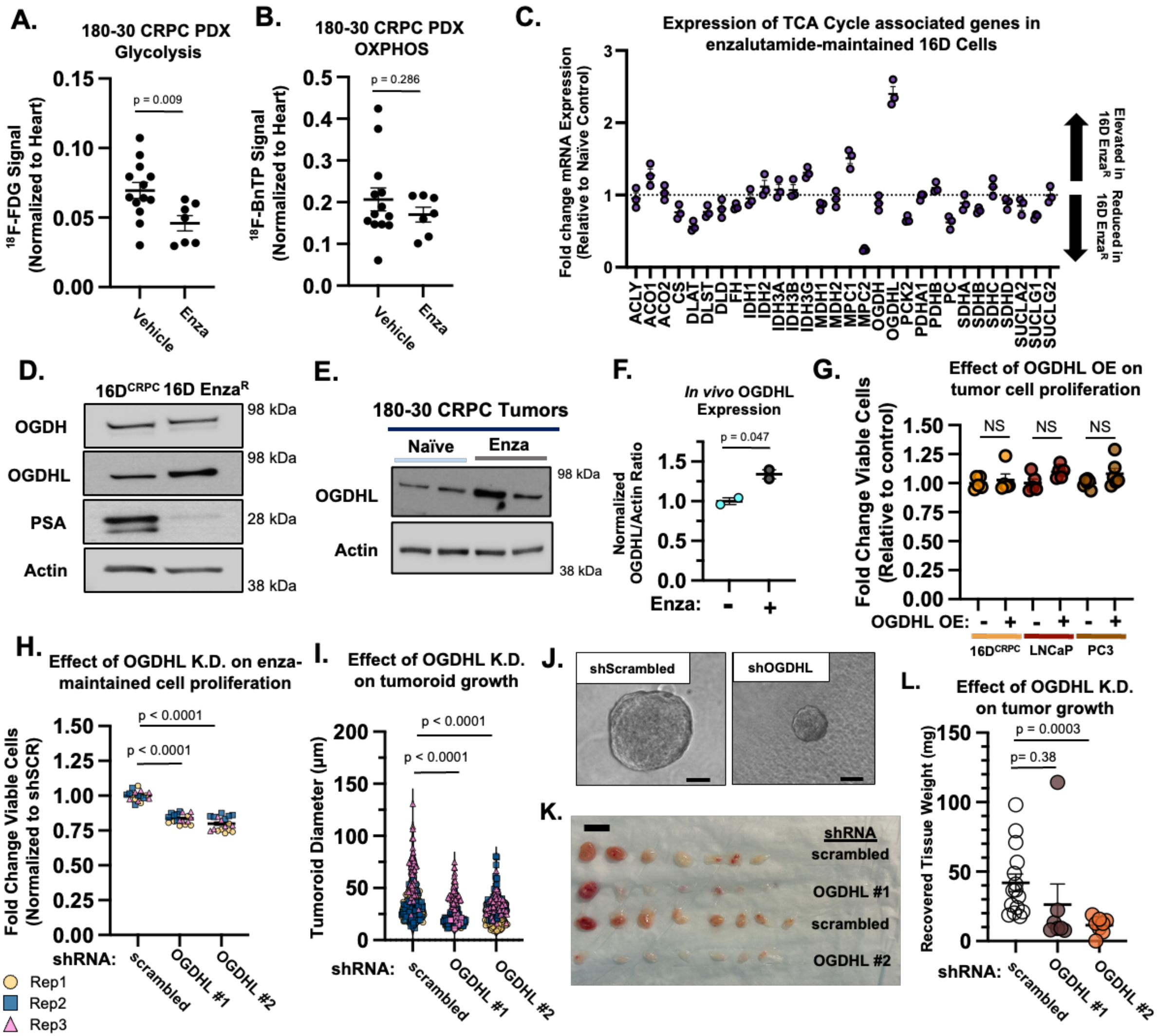
A.
180-30 CRPC PDX Glycolysis
^{18}F-FDG Signal (Normalized to Heart)
p = 0.009
Vehicle
Enza
B.
180-30 CRPC PDX OXPHOS
^{18}F-BnTP Signal (Normalized to Heart)
p = 0.286
Vehicle
Enza
C.
Expression of TCA Cycle associated genes in enzalutamide-maintained 16D Cells
Fold change mRNA Expression (Relative to Naïve Control)
Elevated in 16D Enza^R
Reduced in 16D Enza^R
ACLY ACO1 ACO2 CS DLAT DLST DLD FH IDH1 IDH2 IDH3A IDH3B IDH3G MDH1 MDH2 MPC1 MPC2 OGDH OGDHL PCK2 PDHA1 PDHB PC SDHA SDHB SDHC SDHD SUCLA2 SUCLG1 SUCLG2
D.
16D^{CRPC} 16D Enza^R
OGDH
OGDHL
PSA
Actin
98 kDa
98 kDa
28 kDa
38 kDa
E.
180-30 CRPC Tumors
Naïve
Enza
OGDHL
Actin
98 kDa
38 kDa
F.
In vivo OGDHL Expression
Normalized OGDHL/Actin Ratio
p = 0.047
Enza: - +
G.
Effect of OGDHL OE on tumor cell proliferation
Fold Change Viable Cells (Relative to control)
NS NS NS
OGDHL OE: - + - + - +
16D^{CRPC} LNCaP PC3
H.
Effect of OGDHL K.D. on enza-maintained cell proliferation
Fold Change Viable Cells (Normalized to shSCR)
p < 0.0001
p < 0.0001
shRNA: scrambled OGDHL #1 OGDHL #2
Rep1
Rep2
Rep3
I.
Effect of OGDHL K.D. on tumoroid growth
Tumoroid Diameter (µm)
p < 0.0001
p < 0.0001
shRNA: scrambled OGDHL #1 OGDHL #2
J.
shScrambled
shOGDHL
K.
shRNA
scrambled
OGDHL #1
scrambled
OGDHL #2
L.
Effect of OGDHL K.D. on tumor growth
Recovered Tissue Weight (mg)
p = 0.0003
p= 0.38
shRNA: scrambled OGDHL #1 OGDHL #2

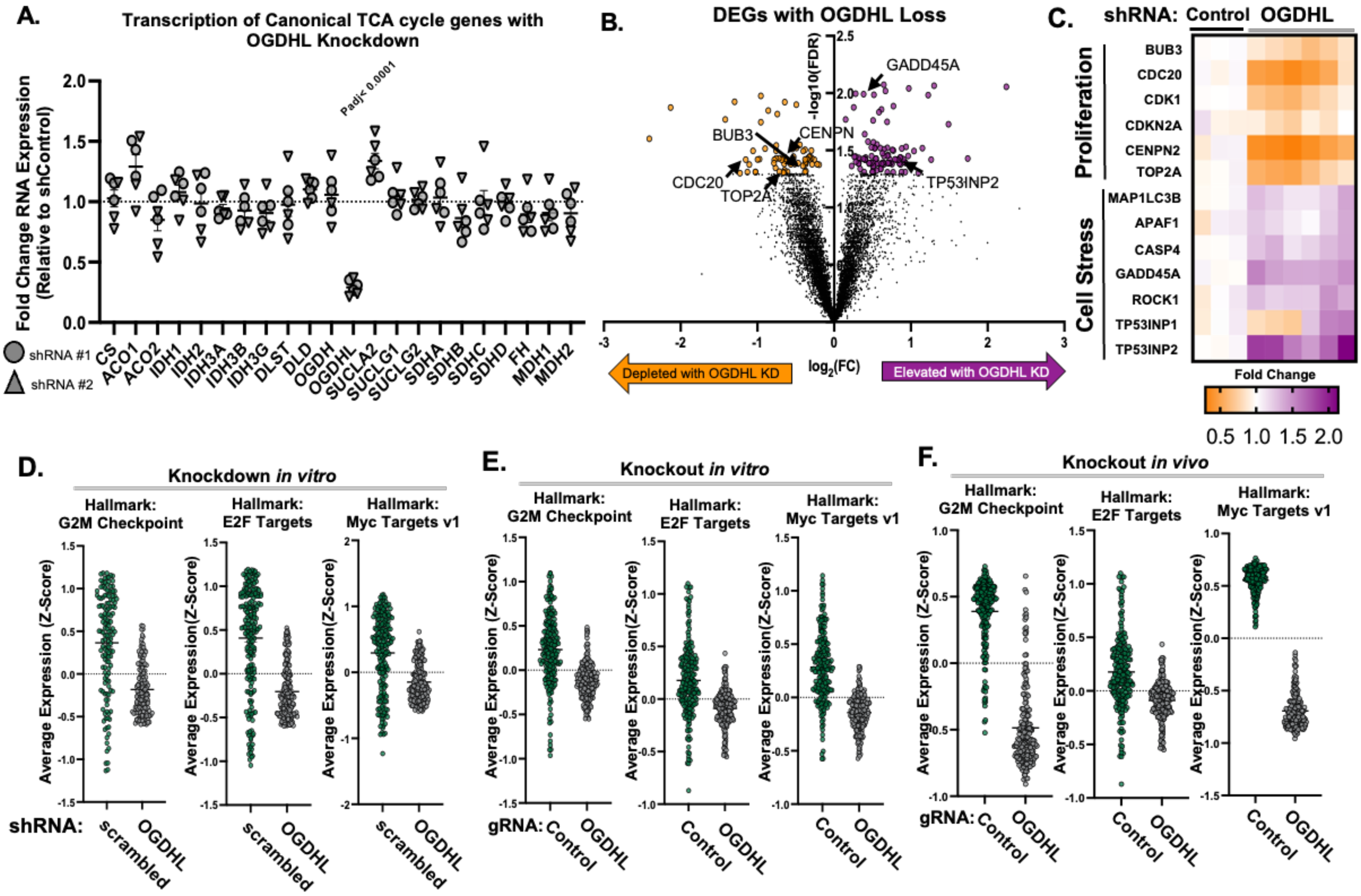
A.
Transcription of Canonical TCA cycle genes with OGDHL Knockdown
Fold Change RNA Expression (Relative to shControl)
Padj< 0.0001
shRNA #1
shRNA #2
CS
ACO1
ACO2
IDH1
IDH2
IDH3A
IDH3B
IDH3G
DLST
DLD
OGDH
OGDHL
SUCLA2
SUCLG1
SUCLG2
SDHA
SDHB
SDHC
SDHD
FH
MDH1
MDH2
B.
DEGs with OGDHL Loss
-log10(FDR)
GADD45A
BUB3
CENPN
CDC20
TOP2A
TP53INP2
Depleted with OGDHL KD
log2(FC)
Elevated with OGDHL KD
C.
shRNA: Control OGDHL
Proliferation
BUB3
CDC20
CDK1
CDKN2A
CENPN2
TOP2A
Cell Stress
MAP1LC3B
APAF1
CASP4
GADD45A
ROCK1
TP53INP1
TP53INP2
Fold Change
0.5 1.0 1.5 2.0
D.
Knockdown in vitro
Hallmark: G2M Checkpoint
Hallmark: E2F Targets
Hallmark: Myc Targets v1
Average Expression (Z-Score)
shRNA: scrambled OGDHL
E.
Knockout in vitro
Hallmark: G2M Checkpoint
Hallmark: E2F Targets
Hallmark: Myc Targets v1
Average Expression (Z-Score)
gRNA: Control OGDHL
F.
Knockout in vivo
Hallmark: G2M Checkpoint
Hallmark: E2F Targets
Hallmark: Myc Targets v1
Average Expression (Z-Score)
gRNA: Control OGDHL

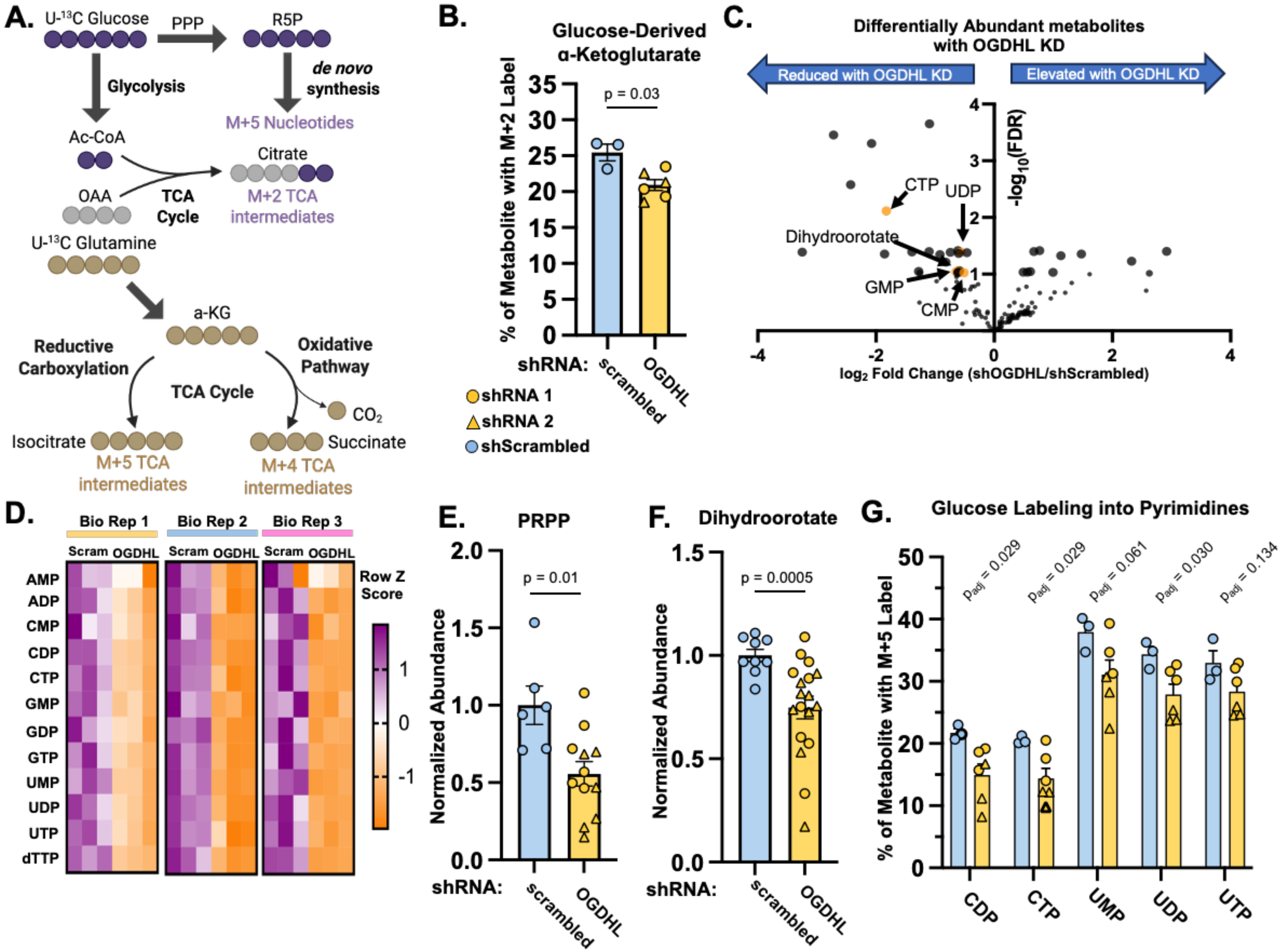
A.
U-13C Glucose
PPP
R5P
Glycolysis
de novo synthesis
M+5 Nucleotides
Ac-CoA
Citrate
OAA
TCA Cycle
M+2 TCA intermediates
U-13C Glutamine
a-KG
Reductive Carboxylation
Oxidative Pathway
TCA Cycle
CO2
Isocitrate
Succinate
M+5 TCA intermediates
M+4 TCA intermediates
B.
Glucose-Derived α-Ketoglutarate
% of Metabolite with M+2 Label
p = 0.03
shRNA:
scrambled
OGDHL
shRNA 1
shRNA 2
shScrambled
C.
Differentially Abundant metabolites with OGDHL KD
Reduced with OGDHL KD
Elevated with OGDHL KD
-log10(FDR)
CTP
UDP
Dihydroorotate
GMP
CMP
log2 Fold Change (shOGDHL/shScrambled)
D.
Bio Rep 1
Bio Rep 2
Bio Rep 3
Scram
OGDHL
AMP
ADP
CMP
CDP
CTP
GMP
GDP
GTP
UMP
UDP
UTP
dTTP
Row Z Score
E.
PRPP
Normalized Abundance
p = 0.01
F.
Dihydroorotate
p = 0.0005
G.
Glucose Labeling into Pyrimidines
% of Metabolite with M+5 Label
padj = 0.029
padj = 0.029
padj = 0.061
padj = 0.030
padj = 0.134
CDP
CTP
UMP
UDP
UTP

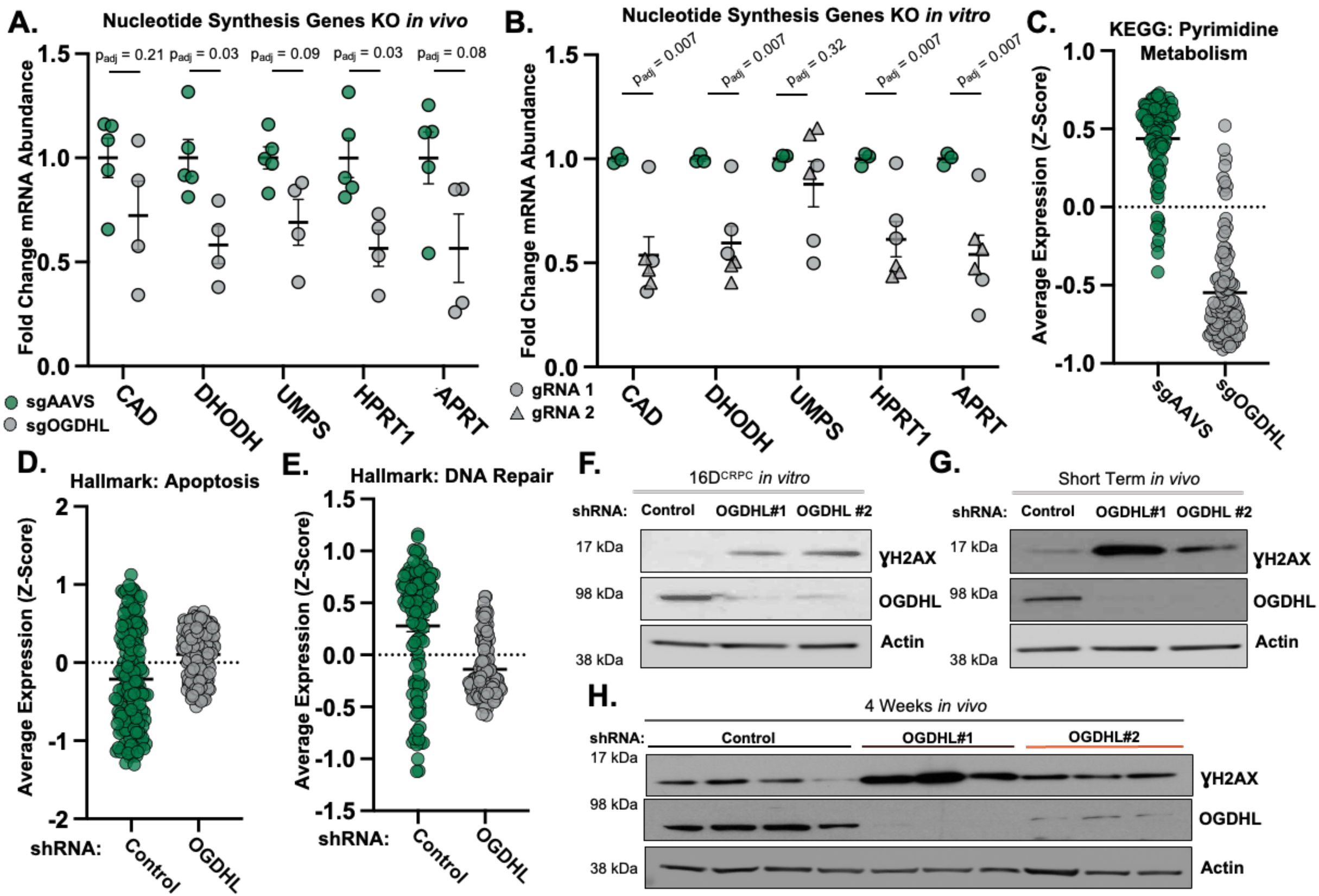
A.
Nucleotide Synthesis Genes KO in vivo
Fold Change mRNA Abundance
padj = 0.21
padj = 0.03
padj = 0.09
padj = 0.03
padj = 0.08
CAD
DHODH
UMPS
HPRT1
APRT
sgAAVS
sgOGDHL
B.
Nucleotide Synthesis Genes KO in vitro
Fold Change mRNA Abundance
padj = 0.007
padj = 0.007
padj = 0.32
padj = 0.007
padj = 0.007
gRNA 1
gRNA 2
C.
KEGG: Pyrimidine Metabolism
Average Expression (Z-Score)
sgAAVS
sgOGDHL
D.
Hallmark: Apoptosis
Average Expression (Z-Score)
shRNA:
Control
OGDHL
E.
Hallmark: DNA Repair
Average Expression (Z-Score)
shRNA:
Control
OGDHL
F.
16D^CRPC in vitro
shRNA:
Control
OGDHL#1
OGDHL #2
17 kDa
98 kDa
38 kDa
γH2AX
OGDHL
Actin
G.
Short Term in vivo
shRNA:
Control
OGDHL#1
OGDHL #2
17 kDa
98 kDa
38 kDa
γH2AX
OGDHL
Actin
H.
4 Weeks in vivo
shRNA:
Control
OGDHL#1
OGDHL#2
17 kDa
98 kDa
38 kDa
γH2AX
OGDHL
Actin

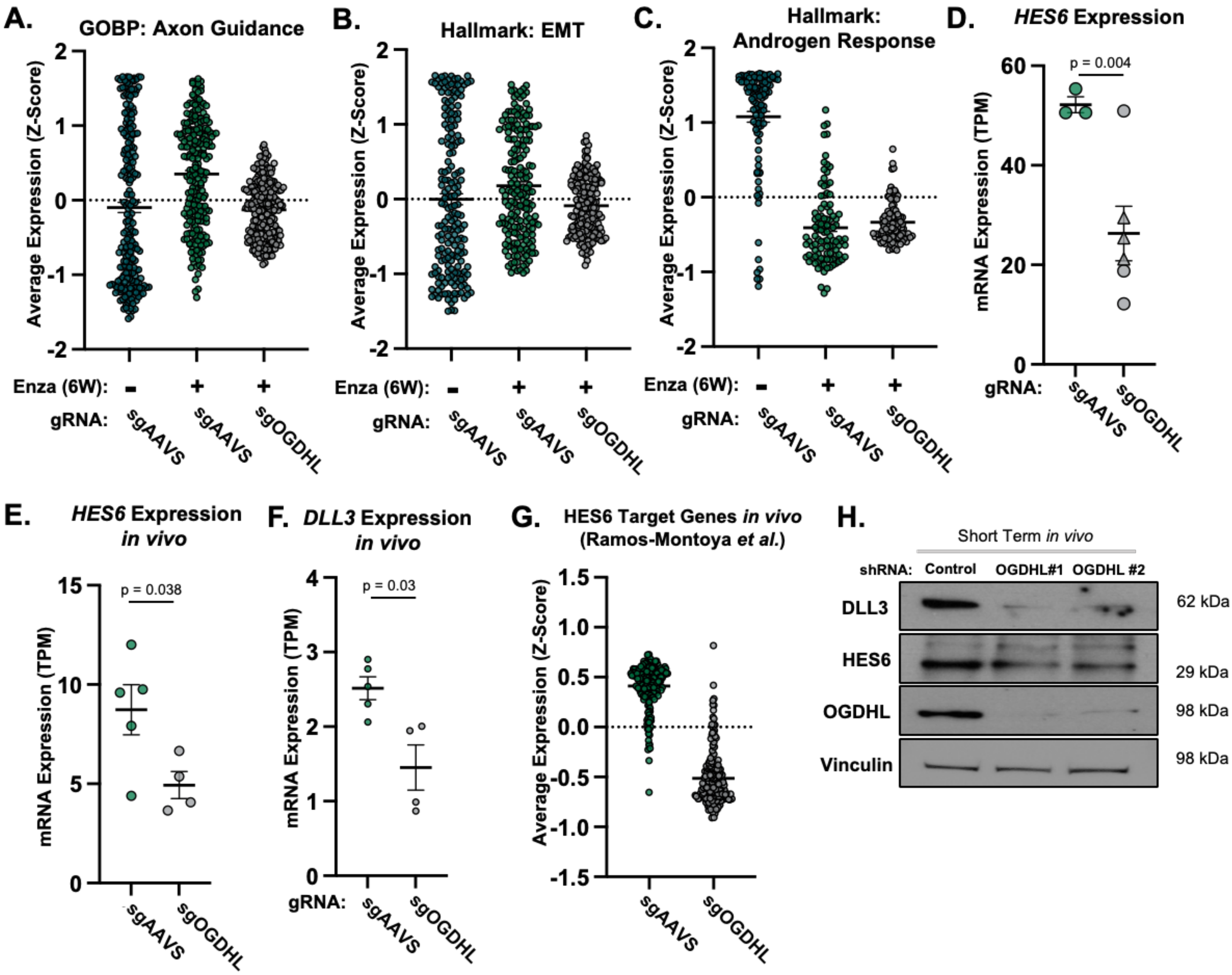
A.
GOBP: Axon Guidance
Average Expression (Z-Score)
Enza (6W): - + +
gRNA: sgAAVS sgAAVS sgOGDHL
B.
Hallmark: EMT
Average Expression (Z-Score)
Enza (6W): - + +
gRNA: sgAAVS sgAAVS sgOGDHL
C.
Hallmark: Androgen Response
Average Expression (Z-Score)
Enza (6W): - + +
gRNA: sgAAVS sgAAVS sgOGDHL
D.
HES6 Expression
p = 0.004
mRNA Expression (TPM)
gRNA: sgAAVS sgOGDHL
E.
HES6 Expression in vivo
p = 0.038
mRNA Expression (TPM)
sgAAVS sgOGDHL
F.
DLL3 Expression in vivo
p = 0.03
mRNA Expression (TPM)
gRNA: sgAAVS sgOGDHL
G.
HES6 Target Genes in vivo (Ramos-Montoya et al.)
Average Expression (Z-Score)
sgAAVS sgOGDHL
H.
Short Term in vivo
shRNA: Control OGDHL#1 OGDHL #2
DLL3 62 kDa
HES6 29 kDa
OGDHL 98 kDa
Vinculin 98 kDa

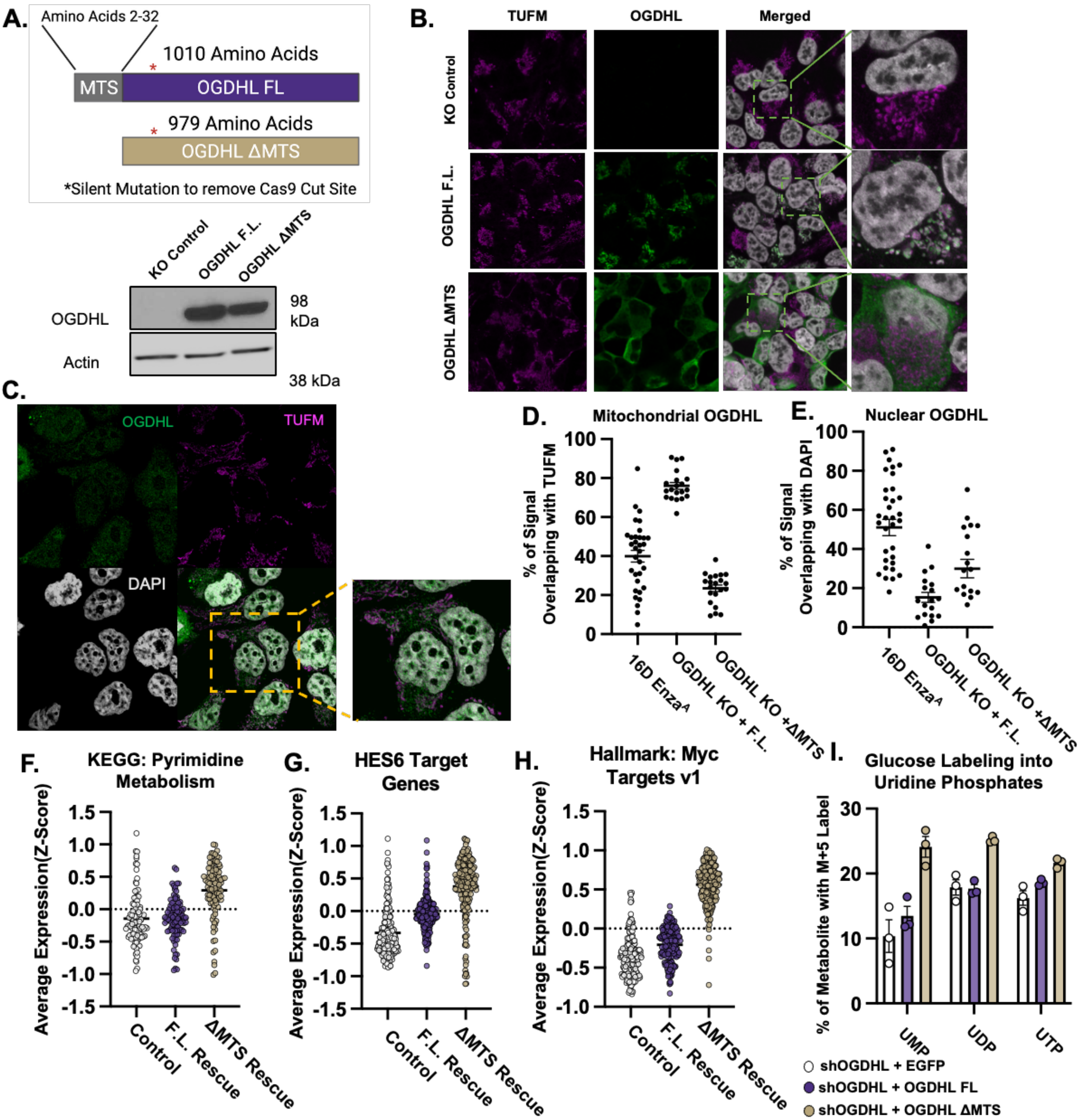
A.
Amino Acids 2-32
1010 Amino Acids
MTS
OGDHL FL
979 Amino Acids
OGDHL ΔMTS
*Silent Mutation to remove Cas9 Cut Site
KO Control
OGDHL F.L.
OGDHL ΔMTS
OGDHL
98 kDa
Actin
38 kDa
B.
TUFM
OGDHL
Merged
KO Control
OGDHL F.L.
OGDHL ΔMTS
C.
OGDHL
TUFM
DAPI
D.
Mitochondrial OGDHL
% of Signal Overlapping with TUFM
16D Enza^A
OGDHL KO + F.L.
OGDHL KO +ΔMTS
E.
Nuclear OGDHL
% of Signal Overlapping with DAPI
F.
KEGG: Pyrimidine Metabolism
Average Expression(Z-Score)
Control
F.L. Rescue
ΔMTS Rescue
G.
HES6 Target Genes
H.
Hallmark: Myc Targets v1
I.
Glucose Labeling into Uridine Phosphates
% of Metabolite with M+5 Label
UMP
UDP
UTP
shOGDHL + EGFP
shOGDHL + OGDHL FL
shOGDHL + OGDHL ΔMTS

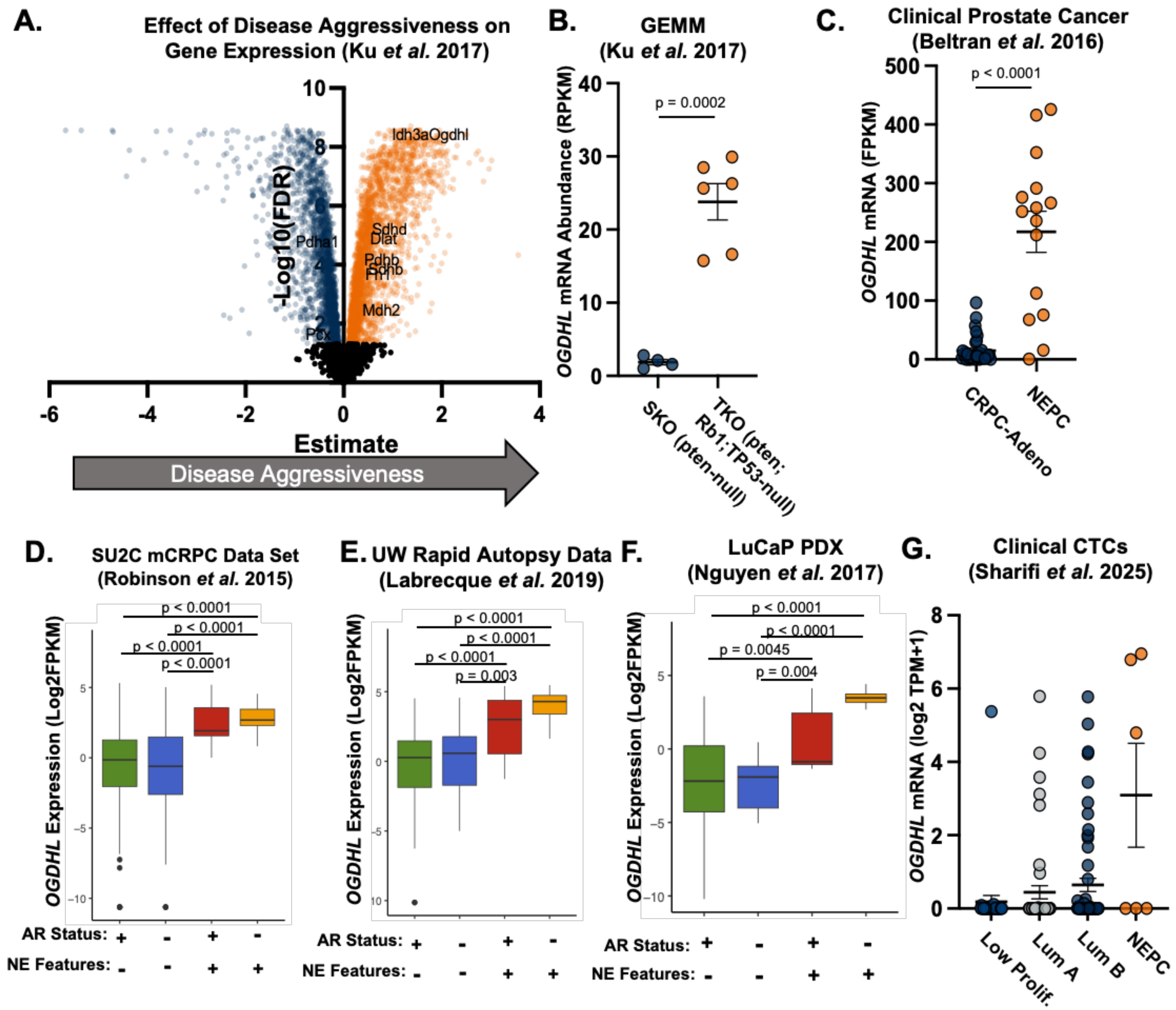
A.
Effect of Disease Aggressiveness on Gene Expression (Ku et al. 2017)
-Log10(FDR)
Estimate
Disease Aggressiveness
Idh3aOgdhl
Sdhd
Dlat
Pdha1
Pdhb
Pdhb
Fh1
Mdh2
Pcx
B.
GEMM (Ku et al. 2017)
OGDHL mRNA Abundance (RPKM)
p = 0.0002
SKO (pten-null)
TKO (pten; Rb1;TP53-null)
C.
Clinical Prostate Cancer (Beltran et al. 2016)
OGDHL mRNA (FPKM)
p < 0.0001
CRPC-Adeno
NEPC
D.
SU2C mCRPC Data Set (Robinson et al. 2015)
E.
UW Rapid Autopsy Data (Labrecque et al. 2019)
F.
LuCaP PDX (Nguyen et al. 2017)
OGDHL Expression (Log2FPKM)
p < 0.0001
p = 0.0045
p = 0.004
p = 0.003
AR Status:
NE Features:
G.
Clinical CTCs (Sharifi et al. 2025)
OGDHL mRNA (log2 TPM+1)
Low Prolif.
Lum A
Lum B
NEPC